1   **Egocentric boundary vector tuning of the retrosplenial cortex**

2

3   Andrew S. Alexander, Lucas C. Carstensen, James R. Hinman, Florian Raudies, G. William
4   Chapman, Michael E. Hasselmo

5

6   Boston University, Center for Systems Neuroscience, Department of Psychological and Brain
7   Sciences, Graduate Program in Neuroscience, 610 Commonwealth Ave. Boston, MA, 022215

8   Correspondence to: Andrew S. Alexander (asalexan@bu.edu) and Michael E. Hasselmo
9   (hasselmo@bu.edu)

10

11

12

13

14

15

16

17

18

19

20

21

22

23

24

25

26

27

28

29

30

31 **Abstract**

32 The retrosplenial cortex is reciprocally connected with a majority of structures implicated in

33 spatial cognition and damage to the region itself produces numerous spatial impairments.

34 However, in many ways the retrosplenial cortex remains understudied. Here, we sought to

35 characterize spatial correlates of neurons within the region during free exploration in two-

36 dimensional environments. We report that a large percentage of retrosplenial cortex neurons

37 have spatial receptive fields that are active when environmental boundaries are positioned at a

38 specific orientation and distance relative to the animal itself. We demonstrate that this vector-

39 based location signal is encoded in egocentric coordinates, localized to the dysgranular

40 retrosplenial sub-region, independent of self-motion, and context invariant. Further, we identify a

41 sub-population of neurons with this response property that are synchronized with the

42 hippocampal theta oscillation. Accordingly, the current work identifies a robust egocentric spatial

43 code in retrosplenial cortex that can facilitate spatial coordinate system transformations and

44 support the anchoring, generation, and utilization of allocentric representations.

45

46

47

48

49

50

51

52

53

54

55

56

57

58

59

60

61

62 **Introduction**

63 Spatial cognition is a critical component of intelligent behavior. The ability to effectively recall

64 and navigate between known goals relies on stored representations of spatial interrelationships.

65 Further, episodic experiences can be thought of as situated within a stored mental map

66 indicating the places in which events occurred (Tulving, 1972). Spatial representations that

67 support both navigation and episodic memory are observed in many brain regions, including the

68 hippocampus (HPC) and medial entorhinal cortex (mEC), where neurons exhibit receptive fields

69 that are correlated with the position or orientation of the animal relative to the array of locations

70 and cues that define the structure of the outside world. This viewpoint-invariant coordinate

71 system is commonly referred to as the allocentric reference frame (O'Keefe and Dostrovsky,

72 1971; Taube et al., 1990ab; Hafting et al., 2005).

73 Although it has been repeatedly shown that intact function of allocentric spatial circuits is critical

74 for spatial memory and navigation (Morris et al., 1982; Taube et al., 1992; Steffenach et al.,

75 2005), it is important to consider that all spatial information enters the brain via sensory organs

76 and their corresponding processing streams. Accordingly, knowledge of the position of a

77 prominent landmark and a neighboring goal location would be, at least initially, incorporated into

78 a stored spatial map in egocentric coordinates relative to the animal itself (Andersen et al.,

79 1983; Andersen et al., 1993; Andersen, 1997; McNamara and Rump, 2003; Burgess, 2006;

80 Byrne et al., 2007; Bicanski and Burgess, 2018). Further, enacting navigational plans can be

81 based upon stored allocentric representations but would ultimately require translation into

82 sequences of actions anchored in an egocentric reference frame (e.g. one turns clockwise

83 relative to their own previous orientation position; Byrne et al., 2007; Whitlock et al., 2008;

84 Bicanski and Burgess, 2018).

85 Neural mechanisms by which egocentric and allocentric coordinate systems are interrelated are

86 still the subject of intense examination. Computational models have predicted that cortical

87 networks capable of integrating allocentric and egocentric information for either constructing or

88 utilizing stored spatial representations require neurons with egocentric sensitivity to external

89 locations (Byrne et al., 2007; Bicanski and Burgess, 2018). Most investigations into egocentric

90 representations in unconstrained animals have focused on the neural substrates of path-

91 integration, a navigational computation wherein self-location is approximated via continuous

92 integration of angular and linear displacement (Mittelstaedt and Mittelstaedt, 1980; McNaughton

93 et al., 2006). Neural correlates of these movement variables have been reported in several

94   structures (McNaughton et al., 1994; Cho and Sharp, 2001; Whitlock et al., 2012; Kropff et al.,

95   2015; Alexander and Nitz, 2015; Hinman et al., 2016; Wilber et al., 2017).

96   Only recently have externally-anchored egocentric representations that extend beyond self-

97   motion been reported (Wilber et al., 2014; Peyrache et al., 2017; Wang, Chen, et al., 2018;

98   Hinman et al., 2019, LaChance et al., 2019). Egocentric representations of this nature may

99   anchor to environmental boundaries. Boundaries present a unique intersection between

100   egocentric and allocentric coordinate systems as they have fixed positions that define the

101   navigable allocentric space and simultaneously restrict the egocentric affordances of the agent

102   such as what can be viewed or what motor plans can be executed. Importantly, environmental

103   bounds or walls extend along large regions of an environment, and thus enable extended

104   interaction from multiple allocentric or egocentric perspectives. Egocentric neural responses

105   have now been reported in multiple areas such as lateral entorhinal cortex (Wang, Chen, et al.,

106   2018), dorsal striatum (Hinman et al., 2019), and postrhinal cortices (LaChance et al., 2019).

107   However, none of these regions possess the reciprocal interconnectivity between egocentric

108   and allocentric spatial circuitry that might mediate bidirectional reference frame transformations.

109   From a connectivity standpoint, the retrosplenial cortex (RSC) is an excellent candidate to

110   examine egocentric representations during navigation. Further, theoretical work has posited that

111   RSC forms a computational hub for supporting coordinate transformations (Byrne et al., 2007;

112   Clark et al., 2018; Rounds et al., 2018; Bicankski and Burgess, 2018). RSC is composed of two

113   interconnected sub-regions, dysgranular (dRSC) and granular (gRSC), which have slightly

114   different connectivity with cortical and subcortical regions (Shibata et al., 2009). dRSC (in mice

115   agranular RSC) is positioned along the dorsal surface of the brain and possesses biased

116   interconnectivity with association, sensory, and motor processing regions that code in

117   egocentric coordinates (Vogt and Miller, 1983; van Groen and Wyss, 1992; Reep et al., 1994;

118   Shibata et al., 2004; Wilber, Clark, et al., 2015; Yamawaki et al., 2016; Olsen et al., 2016;

119   Hovde et al., 2019). In contrast, gRSC has strong reciprocal innervation with the hippocampal

120   formation and associated structures that are primarily sensitive to the allocentric coordinate

121   system (van Groen and Wyss, 1990; Wyss and van Groen, 1992; van Groen and Wyss, 2003;

122   Miyashita and Rockland, 2007; Sugar et al., 2011; Kononenko and Witter, 2012; Czajkowski et

123   al., 2013; Olsen et al., 2017; Yamawaki et al., 2019ab; Haugland et al., 2019).

124   Despite possessing dense reciprocal connectivity with numerous regions known to support

125   spatial cognition, few reports have examined spatial response properties of neurons within the

126   RSC. Most assessments of functional properties of RSC neurons have occurred in rodents

127 performing track running tasks (Smith and Mizumori, 2012; Alexander and Nitz, 2015; Alexander

128 and Nitz, 2017; Vedder et al., 2016; Mao et al., 2017; Mao et al., 2018; Miller et al., 2019). Track

129 running experiments have revealed that RSC neurons exhibit spatial correlates with conjunctive

130 sensitivity to allocentric and egocentric coordinate systems (among others) simultaneously

131 (Alexander and Nitz, 2015). Conjunctive tuning of this type has been shown in modelling work to

132 facilitate spatial coordinate transformations further supporting a role for RSC in the required

133 transformation between these two spatial reference frames (Pouget and Sejnowksi, 1997;

134 Bicanski and Burgess, 2018). However, grid cells, head direction cells, place cells, and other

135 forms of well-characterized spatial receptive fields have primarily been examined in two-

136 dimensional (2D) environments. Only a few experiments have studied RSC in similar conditions

137 and all such reports have focused on head direction encoding (Chen et al., 1994ab; Cho and

138 Sharp, 2001; Jacob et al., 2017).

139 To examine externally-referenced egocentric representations in RSC capable of supporting both

140 navigation and reference frame transformations we recorded from both RSC sub-regions while

141 rats freely explored familiar two-dimensional environments. We report that subsets of RSC

142 neurons exhibit a variety of spatially-stable activation patterns in egocentric and allocentric

143 coordinate systems. These findings support predictions from computational modeling related to

144 translation between spatial reference frames and highlight important navigation related variables

145 encoded in association cortex (Byrne et al., 2007; Bicanski and Burgess, 2018).

146 **Results**

147 ***RSC neurons exhibit stable spatial activity during free exploration***

148 We recorded 555 neurons extracellularly in bilateral retrosplenial cortex (RSC) from male Long-

149 Evans rats (n = 7) during free exploration. To enable comparisons between functional properties

150 of neurons recorded in dysgranular (dRSC) versus granular (gRSC) sub-regions of RSC, we

151 estimated tetrode placement and depth for each session (**Figure 1a,** n = 130 sessions, **sFigure**

152 **1a-b**). Of the total population, 41.5% (n = 230/555) were recorded from dRSC, 15.1% (n =

153 84/555) from the border between dRSC and gRSC, and 43.4% (n = 241/555) within gRSC. For

154 baseline sessions, rats foraged for scattered reward in $1.25m^2$ square arenas with observable

155 fixed distal cues.

156 RSC neurons exhibited complex firing rate fluctuations as rats randomly foraged within open

157 arenas (**Figure 1b**). To assess the spatial stability of these representations for each neuron

158 individually, we began by examining correlations between 2D spatial firing ratemaps constructed

159   from first and second halves of each experimental session (**Figure 1c**). Across the full

160   population of RSC neurons, 47.0% of cells (n = 261/555) had spatial correlations greater than

161   the 99th percentile (ρ = 0.23) of the distribution of correlations observed following 100 random

162   shifts of the complete spike train for each neuron relative to spatial position (**Figure 1c**).

163   In some cases, RSC neurons with spatially anchored responses had slight differences in basic

164   firing properties than those that were not spatially stable (**sFigure 2b**). Of particular interest and

165   consistent with the presence of spatial receptive fields, RSC neurons with spatially reliable

166   activity had significantly greater spatial coherence than non-stable cells (**sFigure 2b-c**).

167   Spatially anchored firing patterns were also observed at more ventral recording sites where it

168   was difficult to resolve whether the recording tetrode was in RSC or the cingulum bundle

169   (**sFigure 2d**). Recordings from these sites were not included in the pool of RSC neurons for

170   analysis.

Egocentric boundary vector responsivity of RSC

172   Of neurons with stable spatial firing in the open field, several had receptive fields that were

173   qualitatively proximal to environmental boundaries (**Figure 1b, right**). Inspection of the

174   relationship between each spike and the movement direction of the animal revealed that these

175   responses manifested when the animal was oriented in a similar manner relative to any wall,

176   suggesting that the receptive field was defined in an egocentric manner. As such, these

177   responses were reminiscent of egocentric boundary cells (EBCs) recently reported in the dorsal

178   striatum (dStr, Hinman et al., 2019), lateral entorhinal cortex (LEC, Wang, Chen, et al., 2018),

179   and postrhinal cortex (POR, LeChance et al., 2019). To test this explicitly we constructed

180   egocentric boundary ratemaps (EBRs) using procedures previously described (Hinman et al.,

181   2019; **Figure 1d**). Briefly, for each behavioral frame, the distance to the nearest wall in each 3°

182   offset from the animal's movement direction was calculated (**Figure 1d**). The same process is

183   repeated for the position of each spike from each neuron, and then ratemaps in polar

184   coordinates were constructed by dividing the number of spikes by the total behavioral

185   occupancy in seconds.

186   From each EBR, we computed the mean resultant length (MRL) of angular tuning as well as the

187   absolute difference in angular tuning direction and distance between first and second halves of

188   the baseline session. RSC cells were determined to exhibit significant egocentric boundary

189   sensitivity if they met the following criteria: 1) they had a MRL for the first and second halves of

190   the session that were greater than the 99th percentile of the distribution of resultants computed

191   following repeated shifted spike train randomizations, 2) had an absolute difference of mean

192   directional tuning between halves of the baseline session that was less than 45 degrees, and 3)

193   had an absolute difference in preferred distance tuning (described below) between halves that

194   was less than 75% of the preferred distance tuning computed from the full baseline session.

195   Using these metrics, 15.0% (n = 83/555) of RSC neurons were determined to be EBCs (**Figure**

196   **1e-g**). When a speed threshold was applied (> 5 cm/s), a greater population of RSC neurons

197   reached EBC criterion (22.9%, n = 127/555), which we utilize for further analyses. Overall,

198   application of a speed threshold increased the mean resultant length for nearly all EBCs (**Figure**

199   **1h**, median MRL difference = 0.02, IQR = 0.01-0.03; Wilcoxon Signed Rank, z = 7.73, p =

200   1.1×10^{-14}). This result suggested that the egocentric receptive field of EBC neurons is defined by

201   the movement direction of the animal rather than head direction, which can be computed even

202   when the animal is motionless. Indeed, when EBCs were assessed using head direction instead

203   of movement direction the MRL significantly dropped (EBCs MRL with MD = 0.13, IQR = 0.10-

204   0.18; EBCs MRL with HD = 0.10, IQR = 0.06-0.14, Wilcoxon sign rank test for zero difference, z

205   = 8.04, p = 8.75×10^{-16}).

Properties of RSC egocentric boundary vector receptive fields

207   Sub-populations of RSC EBCs exhibited either increased or decreased activation when the

208   animal occupied a particular orientation and distance relative to environmental boundaries

209   (**Figure 1e-g**). In accordance with prior literature, we refer to those neurons that were inhibited

210   as inverse EBCs (iEBCs, **Figure 1g**) and neurons with excitatory receptive fields as EBCs

211   (**Figure 1e-f**). K-means clustering on numerous EBC features (see methods) yielded four

212   qualitatively coherent groupings of EBC receptive field sub-types that were characterized post

213   hoc: 1) 24.4% (n=31/127) were animal-proximal with a small receptive field (**Figure 1e, blue**

214   **border**), 2) 33.9% (n=43/127) were animal-distal with a larger and/or potentially noisier

215   receptive field (**Figure 1f, orange border**), 3) 31.5% (n = 40/127) were animal-distal with a

216   larger receptive field (**Figure 1f, yellow border**), and 4) 10.2% (n = 13/127) had large inverted

217   EBC receptive fields (**Figure 1g, purple border**). Principal component analysis (PCA) on this

218   same feature space showed that the first two components accounted for 55.6% and 10.8% of

219   the variability, respectively. A comparison of PCA scores for these two components across all

220   RSC EBCs clustered using K-means did not yield distinct boundaries between sub-populations,

221   instead revealing a continuum of EBC receptive fields (**Figure 1j**).

222   Identification of the center of mass of EBC receptive fields revealed a bimodal distribution of

223   preferred orientations that was best fit by a two component Gaussian mixture model (GMM) with

224   means of 100° (L) and 239° (R) relative to directly in front of the animal (**Figure 1k**; Number of

225   GMM components determined via minimizing AIC). Although EBCs were recorded in both

226   hemispheres there was no obvious relationship between the preferred orientation and the

227   hemisphere in which the neuron was recorded, indicating a lack of lateralization of EBC

228   response properties (**Figure 1k**, inset). The distribution of preferred distances was best

229   described by a four component GMM with means of 11cm, 21cm, 37cm, and 50cm centimeters

230   (**Figure 1l**). The size of EBC receptive fields increased as a function of the preferred distance of

231   the egocentric vector indicating that the resolution of the representation was dependent on

232   proximity to boundaries (**Figure 1m, Spearman's ρ = 0.37, p = 2.57x10^{-5}**). The presence of

233   EBCs with preferred distances distal to the animal suggested that the EBC response property

234   was neither dependent upon physical interaction with arena borders nor could be purely posture

235   related which is known to modulate cortical neurons (Mimica, Dunn, et al., 2019).

236   ***EBC responses are localized within dysgranular RSC but lack topographic organization***

237   Egocentric boundary vector sensitivity was primarily observed in dRSC, where 37.0% (n =

238   85/230) of neurons recorded were classified as EBCs (**sFigure 1c**). In contrast, EBCs were

239   observed in 10.0% (n = 24/241) of gRSC and 21.4% (n =18/84) of intermediary area cells

240   between the two sub-regions (dgRSC, see methods and **sFigure 1a**). By and large, the

241   distribution of EBCs amongst RSC sub-regions was consistent across animals (**sFigure 1c**).

242   The EBC response property was observed across a wide range of A/P coordinates spanning a

243   majority of RSC but possessed no further anatomical organization beyond sub-region specificity

244   (range = 2.9 - 6.8mm relative to bregma, **sFigure 1d**). The distribution of spike waveform widths

245   across all RSC neurons was bimodal with identified EBCs primarily found in the cluster of

246   neurons with longer duration waveforms (**sFigure 1e**, K-means clustering on waveform width,

247   cluster 1 median = 0.18s, IQR = 0.15 - 0.23s, EBCs in cluster 1, n = 15/127, 11.8%; cluster 2

248   median = 0.31s, IQR = 0.21 - 0.34s; EBCs in cluster 2, n = 112/127, 88.2%). Further, EBCs had

249   overall low mean firing rates (**sFigure 1e**, EBCs = 1.68Hz, IQR = 0.96 - 2.72Hz, not-EBCS =

250   3.55Hz, IQR = 1.15 - 8.47Hz)**.** Taken together, the EBC sub-population was determined to be

251   primarily composed of putative principal neurons suggesting that the EBC signal is propagated

252   across RSC sub-regions or into other brain regions.

253   EBCs could often be simultaneously recorded which enabled an analysis of potential

254   topography in the distribution of preferred distance and orientation of the egocentric boundary

255   vector. Overall, 129 pairs of RSC EBCs were co-recorded across 31 sessions. Of these pairs,

256   30.2% (n = 39/129) were recorded on the same tetrode (**sFigure 3a**), while the remaining

257   69.8% of EBC pairs (n = 90/129) were concurrently recorded on different tetrodes (**sFigure 3b**).

258   To assess whether there was organization to preferred orientation and distance as a function of

259   proximity of two EBCs (i.e. observed on same or different tetrodes), we next calculated the

260   difference in receptive field center of mass for both angular and distance components for all

261   pairs. Although the preferred distance of EBCs on the same tetrode was trending towards

262   greater similarity (**sFigure 3c**), neither preferred orientation nor distance was statistically

263   different for EBCs recorded on the same versus different tetrodes (**sFigure 3c-3d,** absolute

264   difference in preferred distance (PD) same tetrode = 7.5cm, IQR = 5 - 21.88cm; absolute

265   difference in PD different tetrode = 12.5cm, IQR = 5 - 22.5cm; Wilcoxon rank sum test, z = -

266   1.16, *p* = 0.24; difference in preferred orientation (PO) same tetrode = 33°, IQR = -43.5 –

267   78.75°; difference in preferred orientation (PO) different tetrode = 34.5°, IQR = -6 – 111°;

268   Wilcoxon rank sum test, z = -0.04, *p* = 0.97). Accordingly, we conclude that there is a lack of

269   topographic organization of egocentric boundary vector tuning in the RSC.

270   ***Egocentric boundary vector tuning in secondary motor cortex and posterior parietal***

271   ***cortex but not medial entorhinal cortex***

272   In 3 animals, a subset of more anterior recording tetrodes were positioned in secondary motor

273   cortex (M2, from bregma: AP: -1.1 to -2.9mm, ML: ±0.8 to 1.2mm) and 56 neurons were

274   recorded there (**sFigure 4a**). Of M2 neurons, 21.4% reached EBC criterion (n = 12/56, **sFigure**

275   **4b**). Similarly, 95 neurons across 5 rats were recorded in posterior parietal cortex (PPC or V2,

276   from bregma: AP: -3.7 to -5.9mm, ML: ±1.5 to 2.4mm) and a sub-population of 9.5% (n = 9/95)

277   reached EBC criterion (**sFigure 4c-d**). EBCs and iEBCs were observed in both structures and

278   receptive fields had similar angular and distance distributions as those observed in RSC

279   (**sFigure 4e-f**). In contrast, only 2.4% (n = 7/297) of medial entorhinal cortex (mEC) neurons

280   recorded in similar conditions reached EBC criterion, indicating that the egocentric vector signal

281   was generally not present within the region (**sFigure 4g,** Wang, Chen, et al., 2018).

282   ***EBC responsivity is not explained by self-motion correlates***

283   In free exploration, spatial locations near environment boundaries uniquely restrict the

284   behavioral affordances of the animal. Many observed EBC receptive fields were proximal to the

285   rat, firing only when the animal was close to boundaries and thus most limited in its possible

286 actions. We next tested whether the manifestation of egocentrically referenced boundary vector

287 tuning was in actuality reflective of self-motion related firing that was stereotyped near borders.

288 We began by constructing self-motion referenced firing rate maps during open field sessions

289 (Chen et al., 1994; Whitlock et al., 2012). The angular difference between movement direction

290 ($\Delta\theta$) and the Euclidian distance in two-dimensional location (Δd) was calculated across a sliding

291 100ms window for every position of the animal throughout a free exploration session (**Figure**

292 **2a**, **left**). These displacement values were converted to Cartesian coordinates referenced to the

293 previous location of the animal at each step, thus producing a map of the distance and direction

294 of movement of the animal for all position samples within the exploration session (**Figure 2a**,

295 **middle and right**).

296 Firing rate as a function of these displacement values are presented for example RSC neurons

297 in **Figure 2c-f**. The zero-line intersection indicates the position of the animal at the beginning of

298 each 100ms window and the x and y-axes reflect displacement in lateral and longitudinal

299 dimensions, respectively. Thus, values to the right of the vertical zero line reflect the activity of

300 the neuron when the animal moved to the right relative to the previous position and direction of

301 its body axis and the distance that the action took the animal is reflected in the position of the

302 value along the y-axis.

303 To quantify the stability of self-motion tuning, we correlated self-motion ratemaps for each

304 neuron that were individually computed from interleaved temporal epochs (1s in duration) within

305 the free exploration session. 15.3% (n = 85/555) of RSC neurons exhibited self-motion related

306 activity that had greater stability than the 95th percentile of the distribution of stability correlation

307 values calculated following permutation tests (**Figure 2b**). Of this sub-population, 28.2% (n =

308 24/85) had firing rate modulation that was biased for leftward or rightward movements (**Figure**

309 **2c**), while 34.1% (n = 29/85) were sensitive to longitudinal movements consistent with speed

310 tuning (**Figure 2d**). Of the EBC population, 19.7% (n = 25/127) met the stability criteria,

311 indicating that a small sub-population of neurons exhibiting egocentric boundary vector tuning

312 had stable self-motion correlates (**Figure 2e**). However, the vast majority of RSC EBCs did not

313 exhibit self-motion correlates confirming that egocentric boundary vector tuning was primarily

314 not an epiphenomenon of movement related activity near borders (**Figure 2f**).

315 Beyond EBCs, the present analysis demonstrated overall limited self-motion tuning in RSC

316 during free exploration. This observation shines new light on previously reported turn-sensitive

317 neurons in RSC during track running tasks (Alexander and Nitz, 2015). In prior work, the

318   magnitude of clockwise or counterclockwise activation during track running was demonstrated

319   to be generally insensitive to the magnitude of angular velocity on a trial-by-trial basis. In

320   combination with the lack of self-motion tuning during free foraging observed here, the results

321   collectively suggest that reported egocentric correlates in RSC are externally-referenced and

322   unrelated to the speed of angular movement.

323   ***Generalized linear models demonstrate robust egocentric vector tuning of RSC EBCs***

324   Self-motion is necessarily conflated with egocentric boundary vector tuning because the

325   response primarily manifested during movement (**Figure 1h-i**). An EBC may exhibit stable firing

326   rate fluctuations as a function of self-motion that are driven by the egocentric boundary vector

327   receptive field, not the action state of the animal. For example, an EBC with a receptive field to

328   the animal's left may also show self-motion tuning for clockwise movements as a result of the

329   animal being more likely to turn clockwise when there is a wall occupying the egocentric

330   receptive field. Yet, the same neuron may not be activated when the animal turns clockwise in

331   other locations within the environment that do not satisfy the egocentric boundary vector. Thus,

332   although initially informative, a different approach was required to tease out the influence of self-

333   motion and other potential spatial covariates on EBC activity patterns.

334   We next implemented a generalized linear model (GLM) framework to predict the probability of

335   spiking at each time point as a function of the relative influence of multiple allocentric, self-

336   motion, or EBC-related predictors (**Figure 3a**). Allocentric predictors included the movement

337   direction of the animal and x- and y-position within the arena. Self-motion related predictors

338   included linear speed and angular displacement (i.e. the differential of animal movement

339   direction in 100ms windows).

340   EBC-related predictors were more complicated as a single position sample or spike possessed

341   relationships to multiple locations along boundaries simultaneously. Accordingly, the EBC

342   predictor could take many forms. To minimize the number of sub-predictors, EBC predictors

343   were composed of the animal's distance and egocentric bearing to the center of the arena.

344   Unlike arena boundaries, the center of the arena is a single coordinate that can be described as

345   a function of individual angular and distance components or their conjunction for each position

346   sample (**sFigure 5a**). Critically, EBCs were found to exhibit robust egocentric bearing and

347   distance tuning to the center of the arena making the predictor a reasonable counterpart to

348   referencing single unit activity to arena walls (**sFigure 5c-d**).

349　To test the impact of each predictor individually, we first generated a complete model fit using

350　the full complement of predictors. Next, we dropped each covariate individually and assessed

351　the decrement to model fit using the difference in Akaike information criterion and corresponding

352　log-likelihood ratio tests (AIC, see methods). **Figure 3b** depicts the proportion of RSC neurons

353　that had significant sensitivity to each individual predictor, split into the sub-populations of cells

354　that were or were not classified as egocentric boundary sensitive using strength of bearing

355　tuning and reliability as above and in previous work (Hinman et al., 2019). GLM output

356　corresponded with the initial identification of EBCs using these metrics. Of EBCs, 81.9% (n =

357　104/127) had significant decrements to model fit when conjunctive EBC predictors were

358　removed from the model (**Figure 3b**).

359　Using the GLM, 70% (n = 89/127) of EBCs were significantly modulated by linear speed, more

360　than doubling the percentage of neurons that were identified as velocity sensitive from self-

361　motion ratemap analyses that utilized a 100ms temporal window (**Figure 2d**). GLM analyses

362　yielded only 12.6% (n = 16/127) of RSC EBCs sensitive to angular displacement, thus further

363　confirming that egocentric boundary vector sensitivity was not epiphenomenal to turning actions

364　near arena bounds.

365　Although neurons previously characterized as possessing egocentric boundary vector tuning

366　were accurately detected with the GLM, numerous other predictors were shown to also

367　significantly co-vary with spiking activity (**Figure 3b**). A number of neurons that were initially

368　characterized as non-EBCs had significant model decrements when the EBC-related predictors

369　were excluded (38.8%, n = 141/363 after removing non-EBC interneurons that had mean firing

370　rates > 15Hz; **Figure 3b**). However, as the GLM will zero-weight a non-contributing predictor,

371　the removal of a single covariate can only serve to decrement model fit while adding a predictor

372　can only improve model fit. Accordingly, a significant log-likelihood test following removal of a

373　predictor does not fully demonstrate the relative impact of that predictor in the full model.

374　We next assessed the overall influence of each predictor class (allocentric, self-motion, and

375　EBC-related) on model fit by constructing a nested GLM, dropping each predictor class, and

376　then making comparisons between resulting model fits (Kraus et al., 2013). **Figure 3c** depicts

377　the difference in model fit (dAIC) for both EBCs and non-EBCs between the full model and

378　reduced models with all allocentric, self-motion, or egocentric boundary predictors removed.

379　Larger dAIC values indicate greater impact of the predictor class within the full model. Models

380　without all allocentric or EBC predictors had significant differences in fit between EBCs and non-

381　EBCs (**Figure 3c**, Kruskal-Wallis, χ^2 = 275.67, p = 1.69x10^{-57}, post-hoc Scheffe tests,

382   p<0.0001). There was no difference between these sub-populations of RSC neurons for the

383   removal of self-motion covariates from the model further supporting that EBCs were not more

384   sensitive to speed or angular displacement than the remainder of the RSC population (**Figure**

385   **3c**, Kruskal-Wallis w/ post-hoc Scheffe tests, p=0.95).

386   A clear divergence emerged in the importance of EBC-related predictors for the EBC and non-

387   EBC sub-populations. As reflected in the difference in magnitude of dAIC, EBC predictors had

388   greater impact than either allocentric or self-motion predictors for the EBC population (**Figure**

389   **3d, blue;** $dAIC_{EBC}$ - $dAIC_{Allo}$ for EBCs = 203.5, IQR = 21 – 475.8; $dAIC_{EBC}$-$dAIC_{SM}$ for EBCs =

390   259.2, IQR = 65.6 – 541.1) than for the non-EBC population which had similar dAIC scores

391   (near 0) for models lacking EBC predictors and other predictor classes (**Figure 3d, gray;**

392   $dAIC_{EBC}$ - $dAIC_{Allo}$ for non-EBCs = -14.9, IQR = -110.4 – 10.2; $dAIC_{EBC}$-$dAIC_{SM}$ for non-EBCs = -

393   1.33, IQR = -29.6 – 26.4). Overall, the impact of EBC-related predictors relative to other

394   predictor classes was significantly greater for EBC versus non-EBC sub-populations ($dAIC_{EBC}$ -

395   $dAIC_{Allo}$ for EBCs versus non-EBCs, Wilcoxon rank sum, z = -10.8, p = 2.51×10^{-27}; $dAIC_{EBC}$-

396   $dAIC_{SM}$ for EBCs versus non-EBCs, Wilcoxon rank sum, z = -12.3, p = 9.33×10^{-35}).

397   This result suggested that although models without allocentric or self-motion predictors could

398   yield significantly decreased model fit, the vast majority of EBC neurons were significantly more

399   impacted by EBC predictors. Two example EBCs in **Figure 3e** illustrate this point, wherein a

400   spike train generated from the output of each model was used to construct trajectory plots and

401   egocentric boundary ratemaps. In both cases, the model lacking egocentric orientation and

402   distance information yields a trajectory plot and egocentric boundary ratemap that is

403   substantially poorer at reconstructing the actual data than any other reduced model.

404   Although egocentric predictors were the dominant influence on EBC activation, nearly all EBCs

405   (98.4%, n = 125/127) were statistically impacted by the removal of more than one predictor

406   category. In this manner the GLM analyses revealed that RSC EBCs were conjunctively

407   sensitive to the position of arena boundaries in egocentric coordinates and allocentric heading

408   or location simultaneously. This feature of EBC responsivity is consistent with theoretical work

409   proposing a transformation between egocentric and allocentric spatial representations within

410   RSC (Bicanski and Burgess, 2018).

411   **GLM confirms vectorial representation**

412   Use of the GLM framework provided an opportunity to verify that RSC neurons with egocentric

413   boundary sensitivity actually formed vector representations of the relationships between

414   environmental boundaries and the animal. By dropping out egocentric bearing and egocentric

415   distance from the model individually, we were able to investigate the relative influence of the

416   individual components of the egocentric boundary vector in isolation for each neuron.

417   Significant model decrements were observed in 100% (n = 127/127) of EBCs following removal

418   of the egocentric bearing component and 74.8% (95/127) of EBCs were impacted by the

419   removal of egocentric distance predictors. Overall, the magnitude of error to model fit was

420   substantially greater when egocentric bearing was removed indicating that, although both

421   distance and orientation components are critical for egocentric boundary vector responsiveness,

422   the directional component more robustly drives neurons exhibiting this tuning preference

423   (**Figure 3f**, difference in dAIC for egocentric bearing versus egocentric distance = 217.2, IQR =

424   77.5 – 440.4; Wilcoxon signed rank test, z = 9.3, p =1.3×10^{-20}).

425   ***EBCs respond to local not distal environmental features***

426   Characterization of EBC properties and self-motion correlates were conducted in baseline

427   sessions in which the open arena remained in a fixed location relative to the experimental room

428   and fixed distal cues therein. We next conducted a series of experimental manipulations of the

429   relationship between the familiar arena and the testing room in order to confirm that EBC

430   response properties were defined by the relationships between environmental boundaries and

431   the animal itself.

432   First, we rotated the open field 45 degrees to maximally disrupt correspondence between arena

433   walls and distal walls or cues present within the recording environment to verify that EBC

434   responses were anchored to local boundaries and not the broader recording room. Under these

435   conditions we recorded a total of 65 RSC neurons (across 4 rats and 14 sessions) of which 40%

436   (n = 26/65) had EBC sensitivity. Consistent with EBC responses being referenced to the rat,

437   receptive fields in rotated arenas maintained the same orientation and distance with respect to

438   the animal, even though arena boundaries now fell along completely different allocentric axes

439   (**Figure 4a-c;** difference between baseline and rotated preferred orientation = 1.5°, IQR = -12 -

440   18°; Wilcoxon sign rank test, z = 0.53, p = 0.59; difference between baseline and rotated

441   preferred distance = 0cm, IQR = -3.75cm – 3.75cm; Wilcoxon sign rank test, z = -0.26, p =

442   0.79). Although vector tuning remained intact, there were slight but significant changes to

443   ratemap coherence between baseline and rotation sessions which suggested that the quality of

444   the egocentric boundary receptive field was decremented across conditions (**Figure 4d**;

445   difference between baseline and rotated ratemap coherence = 0.03, IQR = -0.02 – 0.06;

446   Wilcoxon sign rank test, z = 2.27, p = 0.02).

447   Consistency in tuning could emerge if the allocentric map anchored to local boundaries rather

448   than distal cues. This was not the case as a population of simultaneously recorded head

449   direction cells (HD, n = 4; **Figure 4a, right**) exhibited consistent mean tuning across the rotated

450   and non-rotated conditions (n = median tuning difference = -6.6°, maximum tuning difference -

451   12.4°). Accordingly, arena rotation experiments dissociated the directional component of EBCs

452   from the allocentric reference frame of HD cells.

453   ***EBC responsivity is anchored to boundaries not the center of the environment***

454   RSC EBCs exhibited egocentric vector sensitivity to both arena boundaries and the center of

455   the environment which we utilized to our advantage in GLM analyses (**sFigure 5**). This occurs

456   because arena boundaries have a fixed relationship relative to the center of the environment.

457   Accordingly, an obvious question is whether the egocentric boundary response is in actuality

458   defined as an egocentric vector to the center of the arena. We addressed this possibility by

459   comparing preferred orientation and distance for 10 RSC EBCs (of 33 total RSC neurons from 4

460   rats across 11 sessions) between baseline arenas and open fields expanded up to 1.75m^2

461   (**Figure 4e**).

462   If EBC responses were anchored to boundaries, we anticipated that the orientation and

463   preferred distance would remain consistent across both conditions. Conversely, if the receptive

464   field was defined by a vector to the center of the arena then the distance component of the

465   egocentric boundary vector would remain fixed to this point. In this scenario, the preferred

466   distance would either move away from the animal in expanded arenas or potentially scale with

467   the arena expansion. We observed that the preferred orientation, preferred distance, and

468   ratemap coherence were not altered between baseline and expanded field sessions confirming

469   that EBCs were indeed anchored to boundaries and not the center of the arena (**Figure 4b-d**,

470   difference between baseline and expanded preferred orientation = -4.5°, IQR = -24 - 6°;

471   Wilcoxon sign rank test, signed rank = 19, p = 0.46; difference between baseline and expanded

472   preferred distance = 0cm, IQR = -7.5 – 5cm; Wilcoxon sign rank test, signed rank = 13.5, p =

473   0.56; difference between baseline and rotated ratemap coherence = 0.01, IQR = -0.03 – 0.07;

474   Wilcoxon sign rank test, signed rank = 31, p = 0.77).

475   ***EBC responsivity is stable in novel environments***

476　Neurons within the broader neural spatial circuitry such as grid cells, head direction cells, and

477　place cells, exhibit consistent, albeit remapped, spatial receptive fields in novel environments.

478　We next questioned whether egocentric boundary vector tuned neurons of RSC would exhibit

479　similar stability in their selectivity. We recorded 17 RSC cells including 8 EBCs in familiar then

480　novel environment sessions (**Figure 4f**, 4 rats across 5 sessions). Neither distance nor

481　orientation components of the egocentric boundary vector were altered in the novel environment

482　relative to baseline illustrating that EBCs are not experience dependent and do not remap

483　between environments (**Figure 4b-c**, difference between baseline and novel preferred

484　orientation = 6°, IQR = -6 - 27°; Wilcoxon sign rank test, signed rank = 19, p = 0.47; difference

485　between baseline and novel preferred distance = -2cm, IQR = -20 – 0cm; Wilcoxon sign rank

486　test, signed rank = 2, p = 0.13). Coherence of EBC receptive fields were unchanged between

487　environments providing evidence that the resolution of the egocentric location signal was robust

488　in both familiar and novel arenas (**Figure 4d**; difference between baseline and novel ratemap

489　coherence = 0.02, IQR = 0.00 – 0.08; Wilcoxon sign rank test, signed rank = 27, p = 0.25).

490　***Stability of EBC sub-populations requires physical boundaries***

491　Sensory information originating from multiple modalities likely underlies the egocentric nature of

492　the RSC boundary vector responses. There are two reasons to believe that somatosensation

493　may inform the preferred orientation and distance of a subset of EBCs. First, many RSC

494　neurons with egocentric boundary vector tuning had preferred distances that were proximal to

495　the animal and within or near whisker range (Preferred distance <12cm; 16.5%, n = 21/127;

496　**Figure 1l**). Secondly, the preferred orientation of EBCs spanned all egocentric bearing angles

497　but were biased laterally perhaps reflecting whisker interaction with borders (**Figure 1k**). As

498　such, we questioned whether the presence of a physical boundary was required for EBC spatial

499　tuning and/or particular subsets of EBC receptive fields.

500　To this end, baseline sessions were compared to recordings in environments that were

501　bordered by drop offs with no arena walls (n = 35 neurons from 7 sessions across 3 rats). 29

502　neurons recorded under these conditions exhibited EBC sensitivity in the baseline session

503　(**Figure 5g**). EBCs detected in the baseline session had similar preferred orientations but more

504　distal preferred distances in sessions with no physical walls (**Figure 4b-c**, difference between

505　baseline and no walls preferred orientation = **-**6°, IQR = -70.5 – 19.5°; Wilcoxon sign rank test, z

506　= -0.41, p = 0.68; difference between baseline and no walls preferred distance = -11.3cm, IQR =

507　-28.8 – 2.5cm; Wilcoxon sign rank test, z = -2.4, p = 0.02). Additionally, the overall coherence of

508　the egocentric receptive field was significantly decreased in the absence of physical walls and

509   fewer EBCs were detected in these sessions (**Figure 4d**; difference between baseline and no

510   walls ratemap coherence = 0.10, IQR = -0.00 – 0.23; Wilcoxon sign rank test, z = 3.6, p =

511   0.0003; EBCs with no walls = 51.4%, n = 18/35 versus 29/35). Collectively, these results

512   suggest that the EBC population signal is degraded in the absence of explicit borders.

513   Despite this fact, numerous EBCs sustained their preferred egocentric vector across conditions.

514   To investigate why some neurons were disrupted and not others we next examined the

515   difference in receptive field coherence as a function of baseline preferred orientation and

516   distance. There was no relationship between the preferred orientation of the neuron and the

517   magnitude of degradation of the spatial signal with no physical walls (**Figure 4h**, Circular-linear

518   correlation, ρ = 0.32, p = 0.23). In contrast, the more proximal the egocentric boundary receptive

519   field was to the animal at baseline the more decreased the tuning was in an arena with no

520   physical walls (**Figure 4i**, Spearman's correlation, ρ = -0.39, p = 0.04). Taken together, these

521   results support the idea that the subset of animal-proximal egocentric boundary cells (**Figure**

522   **1e**) may rely on somatosensory interaction with borders, while EBCs with more animal-distal

523   receptive fields (**Figure 1f**) are preserved in environments with no physical walls because they

524   rely on other sensory modalities.

525   ***RSC EBCs are insensitive to environmental geometry which yields a directional***

526   ***representation of environment shape***

527   Boundaries are unique environmental features in that they both restrict navigational affordances

528   and define the spatial structure of the broader environment. Accordingly, the presence of

529   boundary sensitive neurons within RSC indicates that the region is capable of detecting features

530   of environmental geometry. In a square open field like the one utilized for baseline experimental

531   sessions there are two primary defining features of environmental geometry: 1) conjunctions of

532   walls forming 90° corners and, 2) boundaries that are orientated along two-axes of allocentric

533   environmental directions. As such, we questioned if EBCs would maintain their preferred tuning

534   in circular environments that excluded both of these geometric features.

535   We recorded 23 RSC EBCs as animals free foraged in square and circular environments across

536   two experimental sessions each day (**Figure 5a**, total RSC neurons recorded under these

537   conditions = 32 across 4 rats and 8 sessions). As with most other environmental manipulations,

538   EBC boundary vectors were unchanged when the geometry of the environment was altered

539   (**Figure 5b**, difference between square and circle preferred orientation = 5.5°, IQR = -33 – 18°;

540   Wilcoxon sign rank test, z = 0.10, p = 0.92; difference between square and circle preferred

541   distance = 2.5cm, IQR = -2.5 – 7.5cm; Wilcoxon sign rank test, z = 1.92, p = 0.054; difference

542   between square and circle ratemap coherence = 0.002, IQR = -0.03 – 0.08; Wilcoxon sign rank

543   test, z = 0.41, p = 0.68).

544   A striking feature of many EBCs (**Figure 5a, left**), but not all (**Figure 5a, right**), was the

545   structure of movement direction tuning between square and circular environments. As a

546   consequence of consistent egocentric boundary vector tuning in environments of different

547   shapes, EBCs would typically possess four-pronged directional tuning that aligned with the

548   orientation of the walls in square environments (**Figure 5a, left top**). In contrast, the same

549   consistency in EBC tuning yielded directionally uniform tuning in circular environments (**Figure**

550   **5a, left bottom**).

551   **Figure 5c** depicts movement direction tuning plots for the full population of RSC neurons

552   recorded in square and circular arenas. When the mean population movement direction tuning

553   was examined, distinct peaks fell at the four cardinal directions in square arenas but no such

554   peaks were observed in their circular counterparts (**Figure 5c, bottom plots**). We hypothesized

555   that differences between directional tuning, as a consequence of the presence of EBCs, would

556   allow downstream regions to disambiguate environments of different geometries.

557   To test this, we trained a linear classifier on a random 80% of the directional tuning curves from

558   both environments and attempted to predict which environment the other 20% of movement

559   direction tuning curves were recorded within (**Figure 5d,** Linear discriminant classifier, n =

560   10,000 iterations). Consistent with the hypothesis that geometry could be decoded from a

561   population with EBC tuning, the arena could be identified correctly with 67.7% accuracy (IQR =

562   55.6 – 72.2%) which was statistically significant from both statistical chance (Wilcoxon sign rank

563   with 50% accuracy median, z = 78.7, p = 0) and a classifier ran with arena identity randomized

564   (randomized arena identity = 50%; IQR = 44.4 – 55.6%; Wilcoxon rank sum test, z = 76.6, p =

565   0). We conclude that regions possessing egocentric boundary vector tuning may provide

566   punctate directional signals to downstream regions such as the medial entorhinal cortex that

567   can be compared to other directional inputs to inform circuits about environment geometry.

568   **A sub-population of RSC EBCs are theta modulated**

569   In building off of geometry detection in RSC EBC ensembles, a natural next question is how

570   might these egocentric positional signals be integrated within the broader spatial circuity.

571   Previous work has demonstrated that RSC local field potentials feature a prominent theta

572   oscillation during active movement that is strongly coherent with theta rhythms observed in the

573 dorsal hippocampal formation (Borst et al., 1987; Colom et al., 1988; Talk et al., 2004; Koike et

574 al., 2017; Alexander et al., 2018). Spatial representations in regions with strong theta

575 rhythmicity, such as MEC or HPC, are strongly influenced by boundaries and environmental

576 geometry (Muller and Kubie, 1987; Gothard et al., 1996; O'Keefe and Burgess, 1996; Kenaith et

577 al., 2017; Kinsky et al., 2018; Solstadt et al., 2008; Krupic et al., 2015; Krupic et al., 2018). We

578 next questioned whether RSC neurons exhibiting egocentric boundary vector sensitivity were

579 potentially synchronized with these areas via theta oscillations.

580 Consistent with previous work, we observed a strong RSC theta oscillation and that individual

581 RSC neurons engage with the theta oscillation in two primary modes (**Figure 6a-b).** First, a

582 small sub-population of RSC neurons exhibit theta rhythmic spiking (as revealed by

583 autocorrelations of their spike trains) and are phase locked to the locally recorded theta

584 oscillation (**Figure 6b**; 4%, n = 22/555). Second, a larger subset of RSC neurons do not

585 possess consistent theta rhythmic spiking but are phase locked to the theta oscillation (**Figure**

586 **6c**; 27.6%, n = 153/555, see methods). In order to be phase modulated without firing at a theta

587 rhythm, this latter population may transiently engage with the theta oscillation by firing at

588 particular phases after skipping random theta cycles.

589 No EBCs exhibited intrinsically theta rhythmic spiking, but 24.4% of EBCs (n = 31/127) did

590 phase lock to RSC theta oscillations (**Figure 1d**). The strength of theta modulation (mean

591 resultant length, MRL) was significantly greater for theta-modulated non-EBCs than EBCs

592 (**Figure 6e**, non-EBCs MRL = 0.13, IQR 0.10 – 0.19; EBCs MRL = 0.11, IQR = 0.09 – 0.13,

593 Wilcoxon rank sum test, z = 2.09, p = 0.04). Although not significantly different, non-EBC theta-

594 locked RSC neurons were biased to firing during the rising phase of the theta rhythm whereas

595 theta-locked EBCs preferred the falling phase (**Figure 6f**, non-EBCs phase = 3.6 rad, IQR = 1.9

596 – 4.8 rad; EBCs phase = 2.3 rad, IQR = 1.7 – 5.3 rad; Kuiper two-sample test, k = 1134, p = 1).

597 These results confirm that a sub-population of RSC EBCs are phase-locked to theta oscillations

598 present in RSC, consistent with recent modelling work suggesting periodic modulation as a

599 mechanism for comparing current sensory input about the environment against stored spatial

600 representations (Byrne et al., 2007; Hasselmo et al., 2012; Bicanski and Burgess, 2018).

601 ***RSC spatial sensitivity in the open field and during track running***

602 RSC spatial responses have been primary examined during track running paradigms (Smith and

603 Mizumori, 2012; Alexander and Nitz, 2015; Alexander and Nitz, 2017; Vedder et al., 2016; Mao

604 et al., 2017; Mao et al., 2018; Miller et al., 2019). Accordingly, we questioned whether there was

605   any relationship between stable firing correlates in free exploration and route running. To this

606   end, a subset of RSC neurons (n=87 neurons across 3 rats) were recorded in both open field

607   exploration and on track running paradigms (**sFigure 6a**).

608   Consistent with previous work, we observed RSC neurons with activation anchored to track

609   locations associated with turning, start and end locations associated with reward, and non-

610   specific patterns associated with a particular route during track running (**sFigure 6b-c**).

611   Although there was no clear relationship between EBC responsivity and activation during track

612   traversals, there was a strong positive correlation between spatial stability in these two

613   navigational conditions, suggesting a possible sub-circuit within RSC for reliable spatial

614   representation (**sFigure 6d**, open field stability (ρ) = 0.41, IQR = 0.27 - 0.60; track-running

615   stability (ρ) = 0.07, IQR = -0.01 - 0.20; Spearman's rho, r = 0.68, p = 0).

616   **Discussion**

617   ***RSC spatial representations facilitate reference frame transformations***

618   The current data support and extend the functional role of RSC in reference frame

619   transformations. Specifically, the RSC population exhibits sensitivity to multiple spatial

620   coordinate systems, an essential characteristic of circuitry capable of generating such

621   translations. In the current work we report a large subset of spatially reliable neurons that

622   encode the position of boundaries in egocentric coordinates. Referred to as egocentric

623   boundary cells or EBCs, these neurons robustly encoded a vectorial representation of the

624   distance and orientation of any boundary relative to the animal itself (i.e. in an egocentric

625   reference frame; Wang, Chen, et al., 2018; Hinman et al., 2019; LeChance et al., 2019).

626   Egocentric boundary representations are predicted to form a critical component of the

627   coordinate transformation circuit, as the response property could function to inform the broader

628   spatial circuitry about the position of external landmarks in a viewpoint-dependent manner

629   (Byrne et al., 2007; Bicanski and Burgess, 2018).

630   RSC neurons also exhibited multiple forms of allocentric modulation that could be integrated

631   with EBCs or other forms of egocentric information within theta timescales. Nearly half of RSC

632   neurons exhibited reliable and spatially-anchored responses during free foraging behavior.

633   Spatially stable cells had complex 2D spatial representations that in some cases were

634   reminiscent or possibly descended from spatial non-grid cells observed in mEC (Diehl et al.,

635   2017), allocentric boundary vector cells and axis-tuned neurons of dorsal subiculum (Hartley et

636   al. 2000; Lever et al., 2009; Olson et al., 2017), and/or location modulated head direction cells

637   of post-subiculum (Peyrache et al., 2017). A second form of allocentric response was observed

638   in a subset of RSC neurons that exhibit allocentric head direction sensitivity. These forms of

639   allocentric spatial information may be processed or compared with egocentric boundary vector

640   information within theta timescales. Both subsets of neurons exhibited theta phase modulation

641   which is well known to synchronize information processing throughout the broader allocentric

642   spatial circuit.

643   When paired with the unique anatomical connectivity of RSC with both egocentric and

644   allocentric processing regions, the presence of neurons, such as EBCs, that are sensitive to one

645   or more spatial coordinate systems signifies that the region is capable of interrelating external

646   and internal spatial information for the initial construction and use of stored spatial

647   representations. This fact may explain the diversity of impairments observed in spatial

648   navigation, learning, and memory that occur following damage or lesion to the area (Valenstein

649   et al., 1987; Takahasi et al., 1997; Harker and Whishaw, 2002; Vann et al., 2003; Vann and

650   Aggleton, 2004; Vann and Aggleton, 2005; Pothuizen et al., 2008; Keene and Bucci, 2009;

651   Hindley et al., 2014; Elduayen and Save, 2014).

652   ***The RSC egocentric boundary vector code is context-independent which generates a***

653   ***directional code that reflects environment geometry***

654   EBC spatial receptive fields were activated when the animal was positioned with both a specific

655   orientation and distance from an environmental boundary. EBCs maintained their preferred

656   vector tuning preference in rotated arenas, expanded arenas, and novel arenas (**Figure 4**).

657   Accordingly, the EBC signal does not remap across environments, thus providing a stable,

658   context invariant, positional metric.

659   This stability can be contrasted to the vast majority of allocentric representations, such as place

660   cells, grid cells, or head direction cells, that are known to either show global or rate remapping,

661   translations, or rotations between environments (Muller and Kubie, 1987; Bostock et al., 1991;

662   Leutgeb et al., 2005; Yoganarasimha and Knierim, 2006; Fyhn et al., 2007; Leutgeb et al., 2007;

663   Hoydal et al., 2019). In contrast, border cells of mEC and boundary vector cells of dorsal

664   subiculum maintain similar tuning preferences in a context invariant manner analogous to that

665   observed in the EBCs shown here (Solstadt et al., 2008; Lever et al., 2009). It remains to be

666   seen what interactions exist between cells possessing these different types of boundary

667   anchored receptive fields, however the current data suggest that boundary sensitive neurons

668   may provide a foundational map upon which other spatial representations can be situated

669   (Bicanski and Burgess, 2016).

670   Like border and boundary vector cells, RSC EBC vector representations did not remap in

671   environments of different geometries (Solstadt et al., 2008; Lever et al., 2009). However,

672   because EBCs respond in a directionally-dependent manner along every environmental border,

673   the mean directional tuning of the RSC population reflected the shape of the environment

674   (**Figure 5**). Here, we demonstrated that this directional signal could be utilized to distinguish

675   arena shape. Relative positions of boundaries have repeatedly been show to alter or anchor

676   allocentric spatial representations, especially in mEC grid cells and HPC place cells (Muller and

677   Kubie, 1987; Gothard et al., 1996; O'Keefe and Burgess, 1996; Keinath et al., 2017; Keinath et

678   al., 2018; Kinsky et al., 2018; Solstadt et al., 2008; Krupic et al., 2015; Krupic et al., 2018; Julian

679   et al., 2018). mEC receives excitatory projections, both directly and indirectly, from RSC and

680   projects into HPC (Kononenko and Witter, 2012; Czajkowski et al., 2013). We hypothesize that

681   the RSC arena-geometry-related directional signal may serve to provide excitatory drive at

682   specific allocentric head directions to inform the circuit about the relative angles amongst

683   borders.

684   ***Egocentric vector tuning may support route-centric representations of RSC and PPC***

685   Consistent with previous work in dorsal striatum, RSC EBC tuning was strongest during motion

686   and the directional component of egocentric boundary receptive fields was more robustly driven

687   by the movement direction of the animal rather than head direction (Hinman et al., 2019). Taken

688   together, these properties of EBC sensitivity suggest that the positional signal is related to

689   active navigation and the relationship of trajectories through the environment relative to

690   environmental boundaries.

691   RSC and the reciprocally connected PPC have been shown to exhibit activity patterns during

692   track running paradigms that are anchored to the shape of the route itself (Nitz, 2006; Nitz,

693   2012; Alexander and Nitz, 2015; Alexander and Nitz, 2017). Route-referenced activity in these

694   regions could be potentially explained by EBC tuning or in part arise from the integration of EBC

695   responsivity with other spatial covariates. Consistent with this hypothesis, we showed that the

696   sub-population of spatially stable neurons in 2D free foraging (which included large numbers of

697   EBCs) were more likely to exhibit spatially stable representations during track running (**sFigure**

698   **6**).

699   ***EBCs are primarily restricted to the dysgranular RSC***

700   A striking anatomical feature of the EBC population was that it was primarily localized to the

701   dysgranular sub-region of RSC (dRSC). dRSC has connectivity weighted towards egocentric

702   coordinate systems, as it is reciprocally innervated by cortical regions important for processing

703   sensory and motor information as well as association areas such as PPC wherein

704   egocentrically-referenced spatial responses have been observed (McNaughton et al., 1994;

705   Whitlock et al., 2012; Wilber et al., 2014; Wilber et al., 2017). Further, the concentration of EBCs

706   in dRSC is consistent with theoretical work posing a circuit for translating between egocentric

707   and allocentric coordinate systems that includes posterior parietal cortex (PPC), RSC, and the

708   extended hippocampal formation as primary hubs (Byrne et al., 2007; Oess et al., 2017; Rounds

709   et al., 2018; Clark et al., 2018; Bicanski and Burgess, 2018).

710   Of note, dRSC is also known to possess bidirectional head direction cells (BDHD) that respond

711   to local reference frames in multi-compartment environments with distinct contextual cues

712   (Jacob et al., 2017). This sensitivity ultimately yields allocentric directional tuning plots that are

713   bimodal. In the current work, strongly tuned EBCs commonly exhibited quad-modal allocentric

714   directional tuning that was aligned with the four walls of square environments. This similarity in

715   directional tuning response of EBCs and BDHDs and their co-localization in dRSC raises

716   questions as to the nature of the relationship or interactions between these functional sub-

717   populations.

718   One possibility is that neurons in dRSC are prone to represent the locations of spatial

719   landmarks using egocentric vectors and that EBCs and BDHDs are both special cases

720   constrained by their respective experimental setups. In the case of EBCs reported here, the

721   vector may anchor to boundaries because borders are the only landmarks present in the open

722   field that can cause activation of the receptive field. In the work of Jacob et al., the egocentric

723   vector may respond to borders as well as local visual landmarks or doorways between two

724   compartments. The bimodal directional tuning in the latter experiment may arise from

725   constrained egocentric sampling along two-axes as a consequence of the multi-compartment

726   environment segmenting two opposing walls. This proposed egocentric vector encoding of

727   environment features in RSC may underlie functional correlates of local heading orientation,

728   scene processing, or goal location in RSC in humans (Maguire, 2001; Epstein et al., 2007;

729   Epstein et al., 2008; Marchette et al., 2014; Chrastil et al., 2015; Patai et al., 2019).

730   ***A network of vector-based egocentric spatial representation***

731   In addition to RSC, EBCs were also observed in both posterior parietal (PPC) and secondary

732   motor cortices (M2) but not mEC which is commonly thought to represent space in allocentric

733   coordinates. The presence of EBCs in PPC converges nicely with previous work demonstrating

734   egocentric bearing sensitivity of PPC neurons to visual cues positioned along boundaries

735   (Wilber et al., 2014). Computational models exploring circuitry for reference frame

736   transformations and spatial imagery initially predicted EBCs to exist in PPC (Byrne et al., 2007).

737   However, egocentric responses were initially reported in lateral entorhinal cortex, dorsal

738   striatum, and postrhinal cortex, and now here in RSC, PPC, and M2 (Wang, Chen, et al., 2018;

739   Hinman et al., 2019; LeChance et al., 2019; see also, Gofman et al., 2017). Accordingly, a

740   picture of a distributed network of interconnected regions with egocentric vector representations

741   is beginning to emerge. Given the presence of EBCs in several midline structures, it is possible

742   that EBCs are also present in the anterior cingulate cortex as well as thalamic structures that

743   innervate midline associative cortex (Weible et al., 2012; Matulewicz et al., 2019). Future

744   investigations should focus on dependencies amongst the regions currently implicated, as the

745   EBC network may possess functional and anatomical connectivity resembling the well-

746   characterized extended head direction cell network (Taube et al., 2007).

754   **Author Contributions**

755   A.S.A., L.C.C., J.R.H., and M.E.H designed the study. A.S.A and L.C.C. conducted all
756   experiments. A.S.A., F.R., and G.W.C. analyzed the data. A.S.A. and M.E.H wrote the paper. All
757   authors assisted with revision of the manuscript.

758   **Declaration of Interests**

759   The authors declare no competing interests.

760   **References**

761   Alexander, A.S., Nitz, D.A., 2017. Spatially Periodic Activation Patterns of Retrosplenial Cortex
762   Encode Route Sub-spaces and Distance Traveled. Curr. Biol. 27, 1551-1560.e4.
763   https://doi.org/10.1016/j.cub.2017.04.036

764   Alexander, A.S., Nitz, D.A., 2015. Retrosplenial cortex maps the conjunction of internal and
765   external spaces. Nat. Neurosci. 18, 1143–1151. https://doi.org/10.1038/nn.4058

766 Alexander, A.S., Rangel, L.M., Tingley, D., Nitz, D.A., 2018. Neurophysiological signatures of
767 temporal coordination between retrosplenial cortex and the hippocampal formation. Behav.
768 Neurosci. 132, 453–468. https://doi.org/10.1037/bne0000254

769 Andersen, A., Snyder, H., n.d. Coordinate transformations in the representation of spatial
770 information 6.

771 Andersen, R.A., 1997. Multimodal integration for the representation of space in the posterior
772 parietal cortex. Philos. Trans. R. Soc. Lond., B, Biol. Sci. 352, 1421–1428.
773 https://doi.org/10.1098/rstb.1997.0128

774 Andersen, R.A., Mountcastle, V.B., 1983. The influence of the angle of gaze upon the
775 excitability of the light- sensitive neurons of the posterior parietal cortex. J. Neurosci. 3, 532–
776 548.

777 Bicanski, A., Burgess, N., 2018. A neural-level model of spatial memory and imagery. Elife 7.
778 https://doi.org/10.7554/eLife.33752

779 Bicanski, A., Burgess, N., 2016. Environmental Anchoring of Head Direction in a Computational
780 Model of Retrosplenial Cortex. J. Neurosci. 36, 11601–11618.
781 https://doi.org/10.1523/JNEUROSCI.0516-16.2016

782 Borst, J.G., Leung, L.W., MacFabe, D.F., 1987. Electrical activity of the cingulate cortex. II.
783 Cholinergic modulation. Brain Res. 407, 81–93. https://doi.org/10.1016/0006-8993(87)91221-2

784 Bostock, E., Muller, R.U., Kubie, J.L., 1991. Experience-dependent modifications of
785 hippocampal place cell firing. Hippocampus 1, 193–205. https://doi.org/10.1002/hipo.450010207

786 Burgess, N., 2006. Spatial memory: how egocentric and allocentric combine. Trends in
787 Cognitive Sciences 10, 551–557. https://doi.org/10.1016/j.tics.2006.10.005

788 Byrne, P., Becker, S., Burgess, N., 2007. Remembering the past and imagining the future.
789 Psychol Rev 114, 340–375. https://doi.org/10.1037/0033-295X.114.2.340

790 Chen, L.L., Lin, L.H., Barnes, C.A., McNaughton, B.L., 1994a. Head-direction cells in the rat
791 posterior cortex. II. Contributions of visual and ideothetic information to the directional firing. Exp
792 Brain Res 101, 24–34.

793 Chen, L.L., Lin, L.H., Green, E.J., Barnes, C.A., McNaughton, B.L., 1994b. Head-direction cells
794 in the rat posterior cortex. I. Anatomical distribution and behavioral modulation. Exp Brain Res
795 101, 8–23.

796 Cho, J., Sharp, P.E., 2001. Head direction, place, and movement correlates for cells in the rat
797 retrosplenial cortex. Behav. Neurosci. 115, 3–25.

798 Clark, B.J., Simmons, C.M., Berkowitz, L.E., Wilber, A.A., 2018. The retrosplenial-parietal
799 network and reference frame coordination for spatial navigation. Behavioral Neuroscience 132,
800 416–429. https://doi.org/10.1037/bne0000260

801 Colom, L.V., Christie, B.R., Bland, B.H., 1988. Cingulate cell discharge patterns related to
802 hippocampal EEG and their modulation by muscarinic and nicotinic agents. Brain Res. 460,
803 329–338. https://doi.org/10.1016/0006-8993(88)90377-0

804 Czajkowski, R., Sugar, J., Zhang, S.-J., Couey, J.J., Ye, J., Witter, M.P., 2013. Superficially
805 projecting principal neurons in layer V of medial entorhinal cortex in the rat receive excitatory

806   retrosplenial input. J. Neurosci. 33, 15779–15792. https://doi.org/10.1523/JNEUROSCI.2646-
807   13.2013

808   Diehl, G.W., Hon, O.J., Leutgeb, S., Leutgeb, J.K., 2017. Grid and Nongrid Cells in Medial
809   Entorhinal Cortex Represent Spatial Location and Environmental Features with Complementary
810   Coding Schemes. Neuron 94, 83-92.e6. https://doi.org/10.1016/j.neuron.2017.03.004

811   Elduayen, C., Save, E., 2014. The retrosplenial cortex is necessary for path integration in the
812   dark. Behav. Brain Res. 272, 303–307. https://doi.org/10.1016/j.bbr.2014.07.009

813   Epstein, R.A., Higgins, J.S., Jablonski, K., Feiler, A.M., 2007. Visual scene processing in
814   familiar and unfamiliar environments. J. Neurophysiol. 97, 3670–3683.
815   https://doi.org/10.1152/jn.00003.2007

816   Fyhn, M., Hafting, T., Treves, A., Moser, M.-B., Moser, E.I., 2007. Hippocampal remapping and
817   grid realignment in entorhinal cortex. Nature 446, 190–194. https://doi.org/10.1038/nature05601

818   Gofman X., Weiss, S., Rapoport, S., Derdikman, D. (2017). Egocentric border cells upstream of
819   the entorhinal cortex. Society for Neuroscience Abstracts.

820   Gothard, K.M., Skaggs, W.E., McNaughton, B.L., 1996. Dynamics of Mismatch Correction in the
821   Hippocampal Ensemble Code for Space: Interaction between Path Integration and
822   Environmental Cues. J. Neurosci. 16, 8027–8040. https://doi.org/10.1523/JNEUROSCI.16-24-
823   08027.1996

824   Hafting, T., Fyhn, M., Molden, S., Moser, M.-B., Moser, E.I., 2005. Microstructure of a spatial
825   map in the entorhinal cortex. Nature 436, 801–806. https://doi.org/10.1038/nature03721

826   Harker, K.T., Whishaw, I.Q., 2002. Impaired Spatial Performance in Rats with Retrosplenial
827   Lesions: Importance of the Spatial Problem and the Rat Strain in Identifying Lesion Effects in a
828   Swimming Pool. J. Neurosci. 22, 1155–1164. https://doi.org/10.1523/JNEUROSCI.22-03-
829   01155.2002

830   Hartley, T., Burgess, N., Lever, C., Cacucci, F., O'Keefe, J., 2000. Modeling place fields in
831   terms of the cortical inputs to the hippocampus. Hippocampus 10, 369–379.
832   https://doi.org/10.1002/1098-1063(2000)10:4<369::AID-HIPO3>3.0.CO;2-0

833   Haugland, K.G., Sugar, J., Witter, M.P., 2019. Development and topographical organization of
834   projections from the hippocampus and parahippocampus to the retrosplenial cortex. Eur. J.
835   Neurosci. https://doi.org/10.1111/ejn.14395

836   Hindley, E.L., Nelson, A.J.D., Aggleton, J.P., Vann, S.D., 2014. The rat retrosplenial cortex is
837   required when visual cues are used flexibly to determine location. Behavioural Brain Research
838   263, 98–107. https://doi.org/10.1016/j.bbr.2014.01.028

839   Hinman, J.R., Brandon, M.P., Climer, J.R., Chapman, G.W., Hasselmo, M.E., 2016. Multiple
840   Running Speed Signals in Medial Entorhinal Cortex. Neuron 91, 666–679.
841   https://doi.org/10.1016/j.neuron.2016.06.027

842   Hinman, J.R., Chapman, G.W., Hasselmo, M.E., 2019. Neuronal representation of
843   environmental boundaries in egocentric coordinates. Nat Commun 10, 2772.
844   https://doi.org/10.1038/s41467-019-10722-y

845   Hovde, K., Gianatti, M., Witter, M.P., Whitlock, J.R., 2019. Architecture and organization of
846   mouse posterior parietal cortex relative to extrastriate areas. European Journal of Neuroscience
847   49, 1313–1329. https://doi.org/10.1111/ejn.14280

848 Høydal, Ø.A., Skytøen, E.R., Andersson, S.O., Moser, M.-B., Moser, E.I., 2019. Object-vector
849 coding in the medial entorhinal cortex. Nature 568, 400–404. https://doi.org/10.1038/s41586-
850 019-1077-7

851 Jacob, P.-Y., Casali, G., Spieser, L., Page, H., Overington, D., Jeffery, K., 2017. An
852 independent, landmark-dominated head-direction signal in dysgranular retrosplenial cortex. Nat.
853 Neurosci. 20, 173–175. https://doi.org/10.1038/nn.4465

854 Julian, J.B., Keinath, A.T., Frazzetta, G., Epstein, R.A., 2018. Human entorhinal cortex
855 represents visual space using a boundary-anchored grid. Nat. Neurosci. 21, 191–194.
856 https://doi.org/10.1038/s41593-017-0049-1

857 Keene, C.S., Bucci, D.J., 2009. Damage to the retrosplenial cortex produces specific
858 impairments in spatial working memory. Neurobiol Learn Mem 91, 408–414.
859 https://doi.org/10.1016/j.nlm.2008.10.009

860 Keinath, A.T., Epstein, R.A., Balasubramanian, V., 2018. Environmental deformations
861 dynamically shift the grid cell spatial metric. Elife 7. https://doi.org/10.7554/eLife.38169

862 Keinath, A.T., Julian, J.B., Epstein, R.A., Muzzio, I.A., 2017. Environmental Geometry Aligns the
863 Hippocampal Map during Spatial Reorientation. Curr. Biol. 27, 309–317.
864 https://doi.org/10.1016/j.cub.2016.11.046

865 Kinsky, N.R., Sullivan, D.W., Mau, W., Hasselmo, M.E., Eichenbaum, H.B., 2018. Hippocampal
866 Place Fields Maintain a Coherent and Flexible Map across Long Timescales. Curr. Biol. 28,
867 3578-3588.e6. https://doi.org/10.1016/j.cub.2018.09.037

868 Koike, B.D.V., Farias, K.S., Billwiller, F., Almeida-Filho, D., Libourel, P.-A., Tiran-Cappello, A.,
869 Parmentier, R., Blanco, W., Ribeiro, S., Luppi, P.-H., Queiroz, C.M., 2017. Electrophysiological
870 Evidence That the Retrosplenial Cortex Displays a Strong and Specific Activation Phased with
871 Hippocampal Theta during Paradoxical (REM) Sleep. J. Neurosci. 37, 8003–8013.

872 Kononenko, N.L., Witter, M.P., 2012. Presubiculum layer III conveys retrosplenial input to the
873 medial entorhinal cortex. Hippocampus 22, 881–895. https://doi.org/10.1002/hipo.20949

874 Kraus, B.J., Robinson, R.J., White, J.A., Eichenbaum, H., Hasselmo, M.E., 2013. Hippocampal
875 "Time Cells": Time versus Path Integration. Neuron 78, 1090–1101.
876 https://doi.org/10.1016/j.neuron.2013.04.015

877 Kropff, E., Carmichael, J.E., Moser, M.-B., Moser, E.I., 2015. Speed cells in the medial
878 entorhinal cortex. Nature 523, 419–424. https://doi.org/10.1038/nature14622

879 Krupic, J., Bauza, M., Burton, S., Barry, C., O'Keefe, J., 2015. Grid cell symmetry is shaped by
880 environmental geometry. Nature 518, 232–235. https://doi.org/10.1038/nature14153

881 Krupic, J., Bauza, M., Burton, S., O'Keefe, J., 2018. Local transformations of the hippocampal
882 cognitive map. Science 359, 1143–1146. https://doi.org/10.1126/science.aao4960

883 LaChance, P.A., Todd, T.P., Taube, J.S., 2019. A sense of space in postrhinal cortex. Science
884 365, eaax4192. https://doi.org/10.1126/science.aax4192

885 Leutgeb, J.K., Leutgeb, S., Moser, M.-B., Moser, E.I., 2007. Pattern separation in the dentate
886 gyrus and CA3 of the hippocampus. Science 315, 961–966.
887 https://doi.org/10.1126/science.1135801

888 Leutgeb, J.K., Leutgeb, S., Treves, A., Meyer, R., Barnes, C.A., McNaughton, B.L., Moser, M.-
889 B., Moser, E.I., 2005. Progressive Transformation of Hippocampal Neuronal Representations in
890 "Morphed" Environments. Neuron 48, 345–358. https://doi.org/10.1016/j.neuron.2005.09.007

891 Lever, C., Burton, S., Jeewajee, A., O'Keefe, J., Burgess, N., 2009. Boundary Vector Cells in
892 the Subiculum of the Hippocampal Formation. J. Neurosci. 29, 9771–9777.
893 https://doi.org/10.1523/JNEUROSCI.1319-09.2009

894 Maguire, E., 2001. The retrosplenial contribution to human navigation: A review of lesion and
895 neuroimaging findings. Scandinavian Journal of Psychology 42, 225–238.
896 https://doi.org/10.1111/1467-9450.00233

897 Mao, D., Kandler, S., McNaughton, B.L., Bonin, V., 2017. Sparse orthogonal population
898 representation of spatial context in the retrosplenial cortex. Nat Commun 8, 243.
899 https://doi.org/10.1038/s41467-017-00180-9

900 Mao, D., Neumann, A.R., Sun, J., Bonin, V., Mohajerani, M.H., McNaughton, B.L., 2018.
901 Hippocampus-dependent emergence of spatial sequence coding in retrosplenial cortex. Proc.
902 Natl. Acad. Sci. U.S.A. 115, 8015–8018. https://doi.org/10.1073/pnas.1803224115

903 Marchette, S.A., Vass, L.K., Ryan, J., Epstein, R.A., 2014. Anchoring the neural compass:
904 coding of local spatial reference frames in human medial parietal lobe. Nat. Neurosci. 17, 1598–
905 1606. https://doi.org/10.1038/nn.3834

906 Matulewicz, P., Ulrich, K., Islam, M.N., Mathiasen, M.L., Aggleton, J.P., O'Mara, S.M., 2019.
907 Proximal perimeter encoding in the rat rostral thalamus. Scientific Reports 9, 2865.
908 https://doi.org/10.1038/s41598-019-39396-8

909 McNamara, T.P., Rump, B., Werner, S., 2003. Egocentric and geocentric frames of reference in
910 memory of large-scale space. Psychon Bull Rev 10, 589–595.

911 McNaughton, B.L., Battaglia, F.P., Jensen, O., Moser, E.I., Moser, M.-B., 2006. Path integration
912 and the neural basis of the "cognitive map." Nat Rev Neurosci 7, 663–678.
913 https://doi.org/10.1038/nrn1932

914 McNaughton, B.L., Mizumori, S.J., Barnes, C.A., Leonard, B.J., Marquis, M., Green, E.J., 1994.
915 Cortical representation of motion during unrestrained spatial navigation in the rat. Cereb. Cortex
916 4, 27–39.

917 Miller, A.M.P., Mau, W., Smith, D.M., 2019. Retrosplenial Cortical Representations of Space
918 and Future Goal Locations Develop with Learning. Curr. Biol. 29, 2083-2090.e4.
919 https://doi.org/10.1016/j.cub.2019.05.034

920 Mimica, B., Dunn, B.A., Tombaz, T., Bojja, V.P.T.N.C.S., Whitlock, J.R., 2018. Efficient cortical
921 coding of 3D posture in freely behaving rats. Science 362, 584–589.
922 https://doi.org/10.1126/science.aau2013

923 Mittelstaedt, M.-L., Mittelstaedt, H., 1980. Homing by path integration in a mammal.
924 Naturwissenschaften 67, 566–567. https://doi.org/10.1007/BF00450672

925 Miyashita, T., Rockland, K.S., 2007. GABAergic projections from the hippocampus to the
926 retrosplenial cortex in the rat. Eur. J. Neurosci. 26, 1193–1204. https://doi.org/10.1111/j.1460-
927 9568.2007.05745.x

928 Morris, R.G.M., Garrud, P., Rawlins, J.N.P., O'Keefe, J., 1982. Place navigation impaired in rats
929 with hippocampal lesions. Nature 297, 681. https://doi.org/10.1038/297681a0

Muller, R.U., Kubie, J.L., 1987. The effects of changes in the environment on the spatial firing of hippocampal complex-spike cells. J. Neurosci. 7, 1951–1968.

Nitz, D.A., 2012. Spaces within spaces: rat parietal cortex neurons register position across three reference frames. Nat. Neurosci. 15, 1365–1367. https://doi.org/10.1038/nn.3213

Nitz, D.A., 2006. Tracking route progression in the posterior parietal cortex. Neuron 49, 747–756. https://doi.org/10.1016/j.neuron.2006.01.037

Oess, T., Krichmar, J.L., Röhrbein, F., 2017. A Computational Model for Spatial Navigation Based on Reference Frames in the Hippocampus, Retrosplenial Cortex, and Posterior Parietal Cortex. Front. Neurorobot. 11. https://doi.org/10.3389/fnbot.2017.00004

O'Keefe, J., Burgess, N., 1996. Geometric determinants of the place fields of hippocampal neurons. Nature 381, 425. https://doi.org/10.1038/381425a0

O'Keefe, J., Dostrovsky, J., 1971. The hippocampus as a spatial map. Preliminary evidence from unit activity in the freely-moving rat. Brain Res. 34, 171–175. https://doi.org/10.1016/0006-8993(71)90358-1

Olsen, G.M., Ohara, S., Iijima, T., Witter, M.P., 2017. Parahippocampal and retrosplenial connections of rat posterior parietal cortex. Hippocampus 27, 335–358. https://doi.org/10.1002/hipo.22701

Olsen, G.M., Witter, M.P., 2016. Posterior parietal cortex of the rat: Architectural delineation and thalamic differentiation. J. Comp. Neurol. 524, 3774–3809. https://doi.org/10.1002/cne.24032

Olson, J.M., Tongprasearth, K., Nitz, D.A., 2017. Subiculum neurons map the current axis of travel. Nat. Neurosci. 20, 170–172. https://doi.org/10.1038/nn.4464

Patai, E.Z., Javadi, A.-H., Ozubko, J.D., O'Callaghan, A., Ji, S., Robin, J., Grady, C., Winocur, G., Rosenbaum, R.S., Moscovitch, M., Spiers, H.J., 2019. Hippocampal and Retrosplenial Goal Distance Coding After Long-term Consolidation of a Real-World Environment. Cerebral Cortex 29, 2748–2758. https://doi.org/10.1093/cercor/bhz044

Peyrache, A., Schieferstein, N., Buzsáki, G., 2017. Transformation of the head-direction signal into a spatial code. Nat Commun 8, 1752. https://doi.org/10.1038/s41467-017-01908-3

Pothuizen, H.H.J., Aggleton, J.P., Vann, S.D., 2008. Do rats with retrosplenial cortex lesions lack direction? European Journal of Neuroscience 28, 2486–2498. https://doi.org/10.1111/j.1460-9568.2008.06550.x

Reep, R.L., Chandler, H.C., King, V., Corwin, J.V., 1994. Rat posterior parietal cortex: topography of corticocortical and thalamic connections. Exp Brain Res 100, 67–84.

Rounds, E.L., Alexander, A.S., Nitz, D.A., Krichmar, J.L., 2018. Conjunctive coding in an evolved spiking model of retrosplenial cortex. Behav. Neurosci. 132, 430–452. https://doi.org/10.1037/bne0000236

Shibata, H., Honda, Y., Sasaki, H., Naito, J., 2009. Organization of intrinsic connections of the retrosplenial cortex in the rat. Anat Sci Int 84, 280. https://doi.org/10.1007/s12565-009-0035-0

Shibata, H., Kondo, S., Naito, J., 2004. Organization of retrosplenial cortical projections to the anterior cingulate, motor, and prefrontal cortices in the rat. Neuroscience Research 49, 1–11. https://doi.org/10.1016/j.neures.2004.01.005

Smith, D.M., Barredo, J., Mizumori, S.J.Y., 2012. Complimentary roles of the hippocampus and retrosplenial cortex in behavioral context discrimination. Hippocampus 22, 1121–1133. https://doi.org/10.1002/hipo.20958

Solstad, T., Boccara, C.N., Kropff, E., Moser, M.-B., Moser, E.I., 2008. Representation of Geometric Borders in the Entorhinal Cortex. Science 322, 1865–1868. https://doi.org/10.1126/science.1166466

Steffenach, H.-A., Witter, M., Moser, M.-B., Moser, E.I., 2005. Spatial memory in the rat requires the dorsolateral band of the entorhinal cortex. Neuron 45, 301–313. https://doi.org/10.1016/j.neuron.2004.12.044

Sugar, J., Witter, M.P., van Strien, N.M., Cappaert, N.L.M., 2011. The retrosplenial cortex: intrinsic connectivity and connections with the (para)hippocampal region in the rat. An interactive connectome. Front Neuroinform 5, 7. https://doi.org/10.3389/fninf.2011.00007

Takahashi, N., Kawamura, M., Shiota, J., Kasahata, N., Hirayama, K., 1997. Pure topographic disorientation due to right retrosplenial lesion. Neurology 49, 464–469. https://doi.org/10.1212/WNL.49.2.464

Talk, A., Kang, E., Gabriel, M., 2004. Independent generation of theta rhythm in the hippocampus and posterior cingulate cortex. Brain Res. 1015, 15–24. https://doi.org/10.1016/j.brainres.2004.04.051

Taube, J.S., 2007. The Head Direction Signal: Origins and Sensory-Motor Integration. Annual Review of Neuroscience 30, 181–207. https://doi.org/10.1146/annurev.neuro.29.051605.112854

Taube, J.S., 1995. Head direction cells recorded in the anterior thalamic nuclei of freely moving rats. J. Neurosci. 15, 70–86.

Taube, J.S., Kesslak, J.P., Cotman, C.W., 1992. Lesions of the rat postsubiculum impair performance on spatial tasks. Behav. Neural Biol. 57, 131–143.

Taube, J.S., Muller, R.U., Ranck, J.B., 1990a. Head-direction cells recorded from the postsubiculum in freely moving rats. I. Description and quantitative analysis. J. Neurosci. 10, 420–435.

Taube, J.S., Muller, R.U., Ranck, J.B., 1990b. Head-direction cells recorded from the postsubiculum in freely moving rats. II. Effects of environmental manipulations. J. Neurosci. 10, 436–447.

Tulving, E., 1972. Episodic and semantic memory. Organization of memory 1, 381–403.

Valenstein, E., Bowers, D., Verfaellie, M., Heilman, K.M., Day, A., Watson, R.T., 1987. Retrosplenial Amnesia. Brain 110, 1631–1646. https://doi.org/10.1093/brain/110.6.1631

van Groen, T., Michael Wyss, J., 1990. Connections of the retrosplenial granular a cortex in the rat. J. Comp. Neurol. 300, 593–606. https://doi.org/10.1002/cne.903000412

Van Groen, T., Wyss, J.M., 2003. Connections of the retrosplenial granular b cortex in the rat. J. Comp. Neurol. 463, 249–263. https://doi.org/10.1002/cne.10757

van Groen, T., Wyss, J.M., 1992. Connections of the retrosplenial dysgranular cortex in the rat. J. Comp. Neurol. 315, 200–216. https://doi.org/10.1002/cne.903150207

1009 Vann, S.D., Aggleton, J.P., 2005. Selective dysgranular retrosplenial cortex lesions in rats
1010 disrupt allocentric performance of the radial-arm maze task. Behavioral Neuroscience 119,
1011 1682–1686. https://doi.org/10.1037/0735-7044.119.6.1682

1012 Vann, S.D., Aggleton, J.P., 2004. Testing the importance of the retrosplenial guidance system:
1013 effects of different sized retrosplenial cortex lesions on heading direction and spatial working
1014 memory. Behavioural Brain Research 155, 97–108. https://doi.org/10.1016/j.bbr.2004.04.005

1015 Vann, S.D., Kristina Wilton, L.A., Muir, J.L., Aggleton, J.P., 2003. Testing the importance of the
1016 caudal retrosplenial cortex for spatial memory in rats. Behavioural Brain Research 140, 107–
1017 118. https://doi.org/10.1016/S0166-4328(02)00274-7

1018 Vedder, L.C., Miller, A.M.P., Harrison, M.B., Smith, D.M., 2016. Retrosplenial Cortical Neurons
1019 Encode Navigational Cues, Trajectories and Reward Locations During Goal Directed
1020 Navigation. Cereb. Cortex. https://doi.org/10.1093/cercor/bhw192

1021 Vogt, B.A., Miller, M.W., 1983. Cortical connections between rat cingulate cortex and visual,
1022 motor, and postsubicular cortices. J. Comp. Neurol. 216, 192–210.
1023 https://doi.org/10.1002/cne.902160207

1024 Wang, C., Chen, X., Lee, H., Deshmukh, S.S., Yoganarasimha, D., Savelli, F., Knierim, J.J.,
1025 2018. Egocentric coding of external items in the lateral entorhinal cortex. Science 362, 945–949.
1026 https://doi.org/10.1126/science.aau4940

1027 Weible, A.P., Rowland, D.C., Monaghan, C.K., Wolfgang, N.T., Kentros, C.G., 2012. Neural
1028 Correlates of Long-Term Object Memory in the Mouse Anterior Cingulate Cortex. J. Neurosci.
1029 32, 5598–5608. https://doi.org/10.1523/JNEUROSCI.5265-11.2012

1030 Whitlock, J.R., Pfuhl, G., Dagslott, N., Moser, M.-B., Moser, E.I., 2012. Functional split between
1031 parietal and entorhinal cortices in the rat. Neuron 73, 789–802.
1032 https://doi.org/10.1016/j.neuron.2011.12.028

1033 Whitlock, J.R., Sutherland, R.J., Witter, M.P., Moser, M.-B., Moser, E.I., 2008. Navigating from
1034 hippocampus to parietal cortex. PNAS 105, 14755–14762.
1035 https://doi.org/10.1073/pnas.0804216105

1036 Wilber, A.A., Clark, B.J., Demecha, A.J., Mesina, L., Vos, J.M., McNaughton, B.L., 2015.
1037 Cortical connectivity maps reveal anatomically distinct areas in the parietal cortex of the rat.
1038 Front. Neural Circuits 8. https://doi.org/10.3389/fncir.2014.00146

1039 Wilber, A.A., Clark, B.J., Forster, T.C., Tatsuno, M., McNaughton, B.L., 2014. Interaction of
1040 egocentric and world-centered reference frames in the rat posterior parietal cortex. J. Neurosci.
1041 34, 5431–5446. https://doi.org/10.1523/JNEUROSCI.0511-14.2014

1042 Wilber, A.A., Skelin, I., Wu, W., McNaughton, B.L., 2017. Laminar Organization of Encoding and
1043 Memory Reactivation in the Parietal Cortex. Neuron 95, 1406-1419.e5.
1044 https://doi.org/10.1016/j.neuron.2017.08.033

1045 Wyss, J.M., Van Groen, T., 1992. Connections between the retrosplenial cortex and the
1046 hippocampal formation in the rat: A review. Hippocampus 2, 1–11.
1047 https://doi.org/10.1002/hipo.450020102

1048 Yamawaki, N., Corcoran, K.A., Guedea, A.L., Shepherd, G.M.G., Radulovic, J., 2019a.
1049 Differential Contributions of Glutamatergic Hippocampal→Retrosplenial Cortical Projections to
1050 the Formation and Persistence of Context Memories. Cereb. Cortex 29, 2728–2736.
1051 https://doi.org/10.1093/cercor/bhy142

1052   Yamawaki, N., Li, X., Lambot, L., Ren, L.Y., Radulovic, J., Shepherd, G.M.G., 2019b. Long-
1053   range inhibitory intersection of a retrosplenial thalamocortical circuit by apical tuft-targeting CA1
1054   neurons. Nat. Neurosci. 22, 618–626. https://doi.org/10.1038/s41593-019-0355-x

1055   Yamawaki, N., Radulovic, J., Shepherd, G.M.G., 2016. A Corticocortical Circuit Directly Links
1056   Retrosplenial Cortex to M2 in the Mouse. J. Neurosci. 36, 9365–9374.
1057   https://doi.org/10.1523/JNEUROSCI.1099-16.2016

1058   Yoganarasimha, D., Yu, X., Knierim, J.J., 2006. Head Direction Cell Representations Maintain
1059   Internal Coherence during Conflicting Proximal and Distal Cue Rotations: Comparison with
1060   Hippocampal Place Cells. J. Neurosci. 26, 622–631. https://doi.org/10.1523/JNEUROSCI.3885-
1061   05.2006

1062

1063

1064

1065

1066

1067

1068

1069

1070

1071

1072

1073

1074

1075

1076

1077 **Figures**
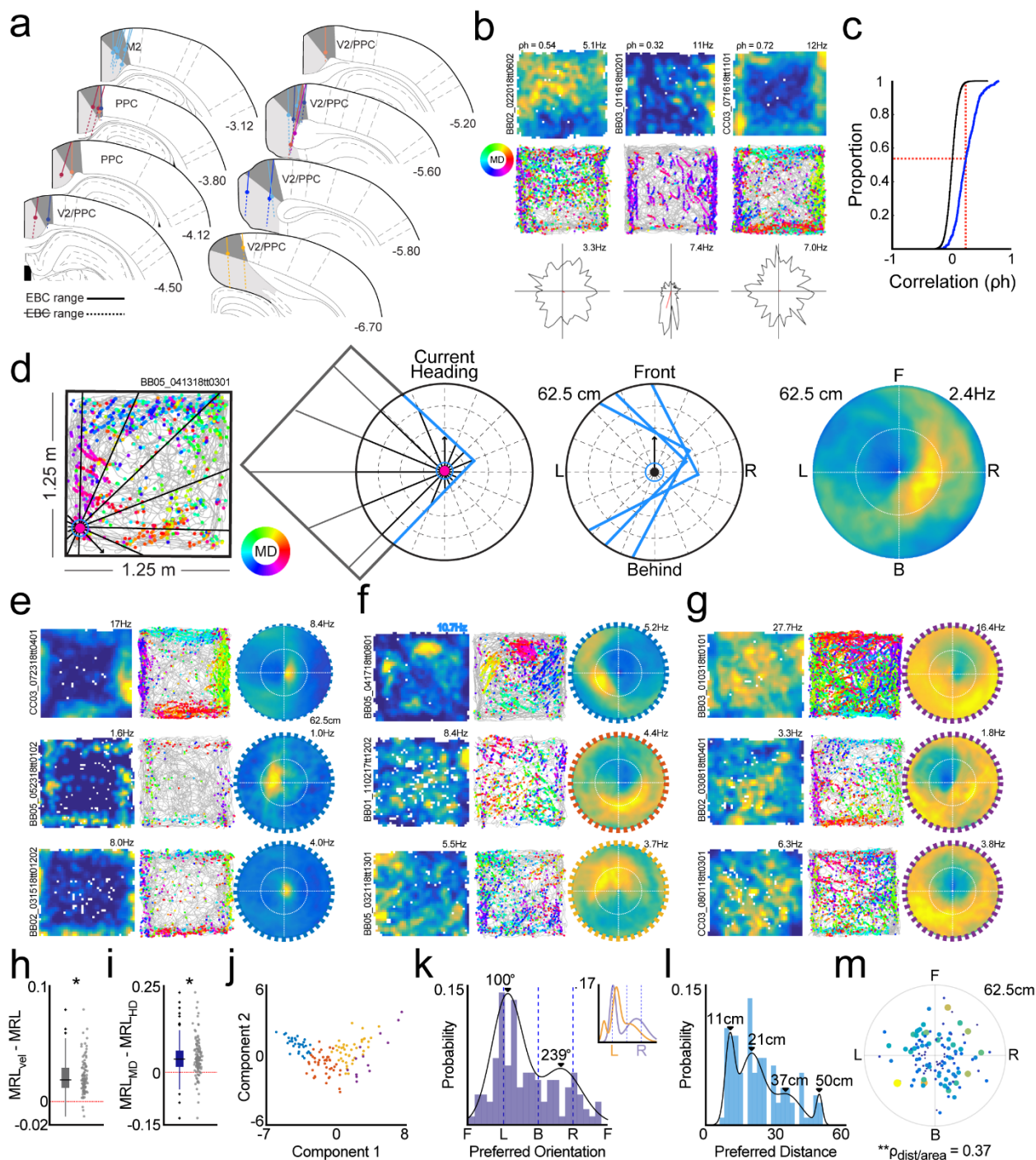
1078 **Figure 1. Egocentric boundary vector representations of RSC neurons during free**
1079 **exploration. a**. Locations of RSC tetrode tracts where neurons with egocentric boundary
1080 sensitivity were observed. For each tetrode, solid lines indicate range where EBCs were
1081 recorded and filled circles indicate most ventral location of EBC observation. **b.** Example two-
1082 dimensional ratemaps (top), trajectory plots (middle), and head direction tuning plots (bottom)
1083 for three RSC neurons with significant stability in spatial firing. For trajectory plots, the position
1084 of the animal throughout the entire experimental session is depicted in gray. The location of

1085   individual spikes are shown with colored circles which indicate the corresponding movement
1086   direction of the animal according to the legend on the left. **c.** Cumulative density function depicts
1087   Spearman's rho calculated after correlating 2D ratemaps taken from the first and second halves
1088   of each experimental session (blue). In black, distribution of spatial stability scores after
1089   randomly shifting spike trains relative to position. Red vertical line shows 99th percentile of
1090   randomized distribution and its intersection with the real distribution of spatial stability.
1091   Percentage of neurons above red horizontal line have significant spatial stability. **d.** Schematic
1092   for construction of egocentric boundary ratemaps (EBRs). Left and middle panels, an example
1093   spike is mapped with respect to egocentric boundary locations in polar coordinates. Left, the
1094   movement direction of the animal is determined for each spike (vector with arrow) and the
1095   distance to wall intersections for all 360° are determined (sub-sample shown for clarity). Middle
1096   left, boundaries within 62.5cm are referenced to the current movement direction of the animal
1097   for a single spike. Middle right, example boundary positions for three spikes. Right, example
1098   egocentric boundary ratemap (EBR). **e.** Two-dimensional ratemaps, trajectory plots, and
1099   egocentric boundary ratemaps for 3 example RSC EBCs with animal-proximal receptive fields.
1100   **f.** Same as in e, but for 3 RSC EBCs with animal-distal receptive fields. **g.** Same as in **e** and **f**,
1101   but for 3 RSC EBCs with inverse receptive fields. **h.** Difference in strength (mean resultant
1102   length, MRL) of EBC tuning when a speed threshold was applied (MRL_{vel}) versus no speed
1103   threshold (MRL). **i.** Difference in strength of EBC tuning when egocentric bearing was
1104   referenced to movement direction (MRL_{MD}) rather than head direction (MRL_{HD}). **j.** For neurons
1105   with significant egocentric boundary vector tuning, a scatter plot of first two principal component
1106   (PCA) scores calculated on multiple features of egocentric boundary ratemaps. Colors show 4
1107   subsets of EBCs determined from K-means clustering on the same feature space as PCA and
1108   correspond to the colored boundaries around EBRs in **e-g**. **k.** Histogram of preferred orientation
1109   of receptive field across all RSC EBCs. Black line, probability density estimate from two-
1110   component Gaussian mixture model (GMM) on distribution of preferred orientation. Black
1111   triangles indicate peaks in GMM estimate. **l.** Same as **k**, but for preferred distance of all RSC
1112   EBC receptive fields. **m.** Polar scatter plot of preferred orientation versus preferred distance for
1113   the full RSC EBC population. Circle size indicates the area of the egocentric boundary vector
1114   receptive field.
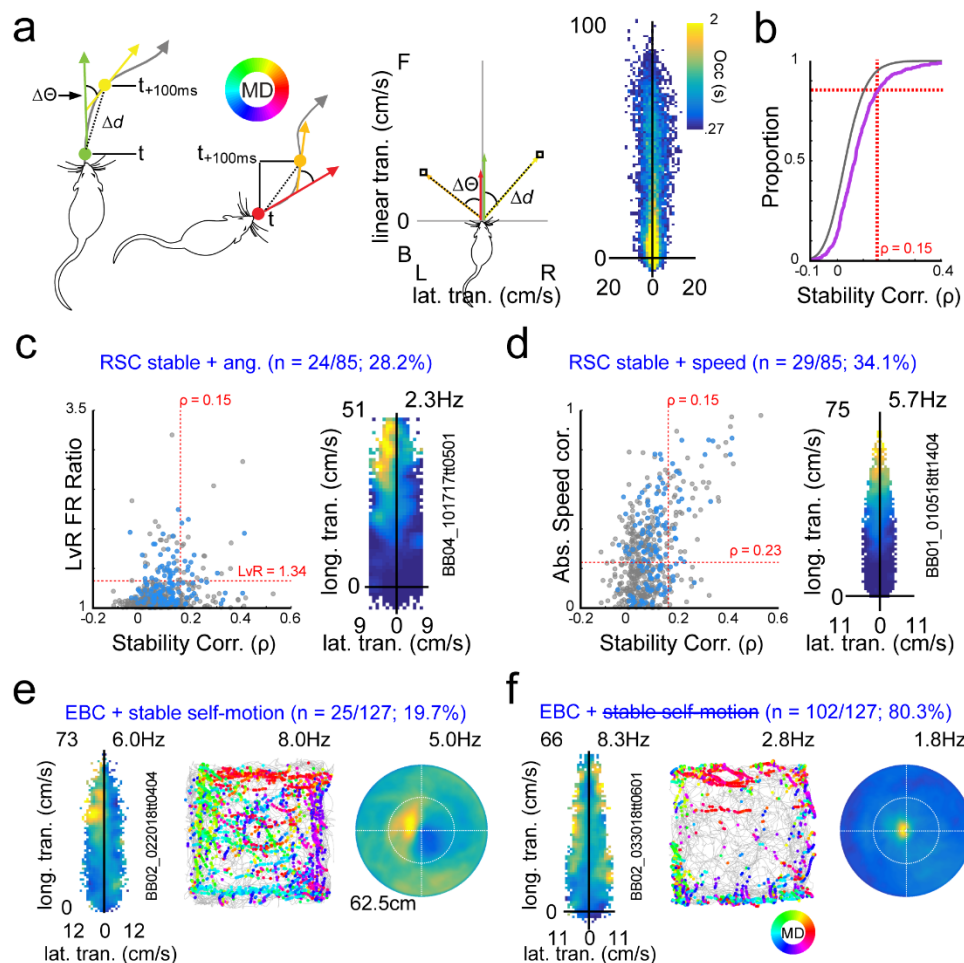
1115

1116

1117

1118

1119

1120

1121

1122

1123

1124

1125

Figure 2. RSC egocentric boundary vector representations cannot be explained purely by self-motion correlates. a. Schematic of generation of self-motion referenced ratemaps. Left, example angular and distance displacements across 100ms temporal windows for two hypothetical position samples. Middle, corresponding lateral and longitudinal displacement for left examples in self-motion referenced coordinates. Right, heat map depicting mean occupancy in seconds for lateral and longitudinal displacement combinations across a complete experimental session. **b.** In pink, cumulative density functions for self-motion ratemap stability values (Spearman's ρ) for all RSC neurons (randomization in gray). Red vertical line shows 95th percentile of randomized distribution and its intersection with the real distribution of spatial stability. Percentage of neurons above red horizontal line have significant spatial stability. **c.** Left, spatial stability score (x-axis) versus absolute ratio of activity on left versus right halves of self-motion ratemaps (y-axis) for all RSC neurons. Blue dots correspond to identified RSC EBCs. Red lines and corresponding values correspond to 99th percentiles of randomized distributions for both metrics. Neurons with values in upper right region were determined to have significant angular displacement tuning. Right, example RSC neuron with significant firing rate modulation for counterclockwise movements. **d.** On left, same as in **c**, but for spatial stability score versus absolute correlation between mean firing rate and animal speed. Right, example RSC neuron with significant firing rate modulation as a function of animal speed. **e.** Example RSC EBC with stable self-motion correlates. **f.** Example RSC EBC with non-stable self-motion correlates.
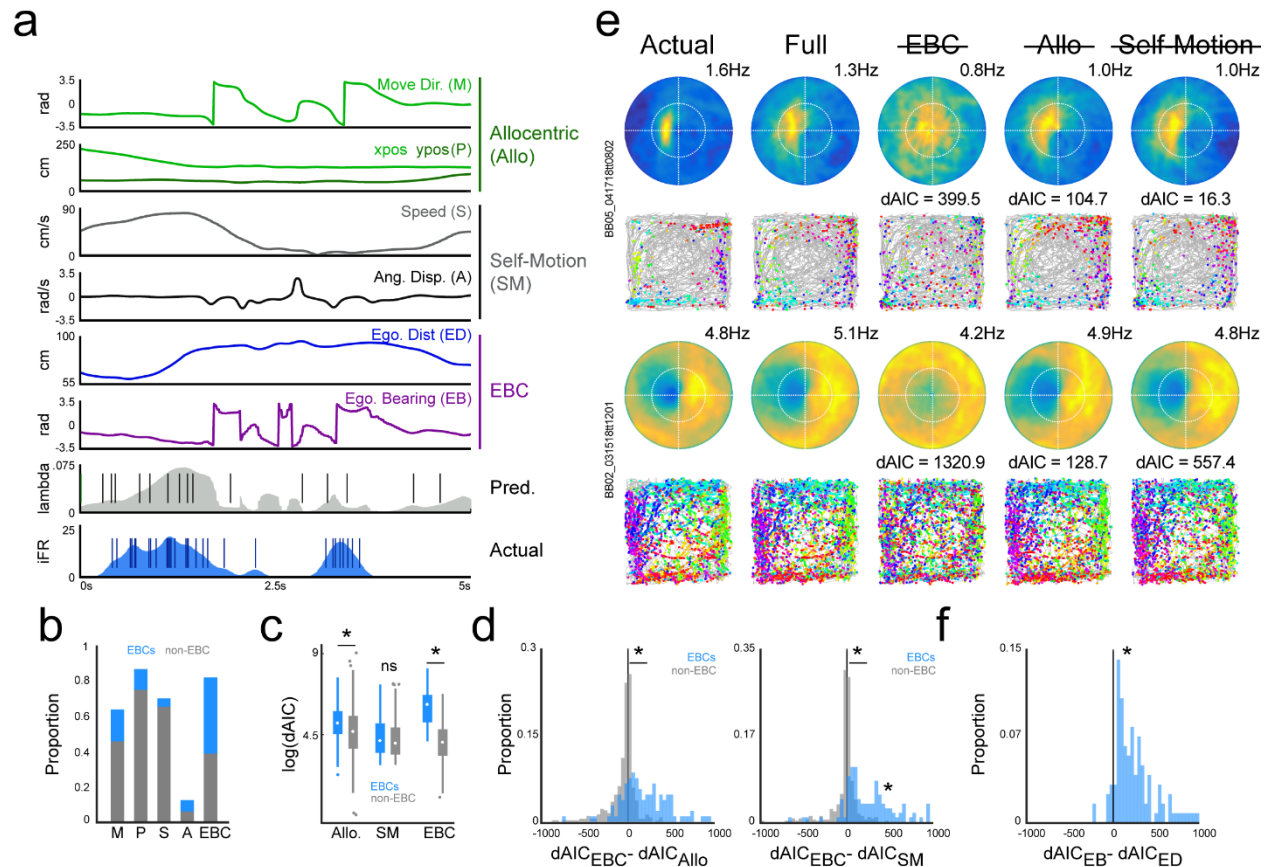
Figure 3. Egocentric vector tuning is more robust than allocentric or self-motion correlates using a generalized linear modelling framework. a. Example GLM predictors composing allocentric, self-motion, and egocentric vector classes with corresponding actual and predicted firing rates and spike trains over a five second window. **b.** Proportion of non-EBC RSC neurons (gray) and EBC RSC neurons (blue) exhibiting significant sensitivity to each predictor individually. M, movement direction; P, x- and y- position; S, speed; A, angular displacement; EBC, egocentric boundary. **c.** Boxplots depicting median and quartiles of log-transformed difference of Akaike information criteria scores (dAIC) for models with all allocentric, self-motion, or egocentric vector predictors removed (blue bars, EBCs; gray bars, non-EBCs). Larger dAICs indicate greater error in model fit with removal of a predictor class. **d.** Comparison of dAIC scores for models with egocentric vector versus allocentric predictors removed (left) or egocentric vector versus self-motion predictors removed (right) for EBCs (blue) and non-EBCs (gray). Rightward shifts indicate greater error in model fit for models with removed egocentric vector predictors. **e.** For two example RSC EBCs, predicted GLM spike trains from all models were utilized to construct egocentric boundary ratemaps and trajectory plots. Left column, actual egocentric boundary ratemap and corresponding trajectory plot. Second column, for the same cell, an egocentric boundary ratemap and corresponding trajectory plot for the generalized linear model constructed using all egocentric vector, allocentric, and self-motion predictors. Final three columns, egocentric boundary ratemaps and trajectory plots for each reduced model and corresponding dAIC scores. **f.** Comparison of dAIC scores for models with the egocentric bearing versus the egocentric distance removed reveal greater impact of egocentric bearing for EBCs.

37
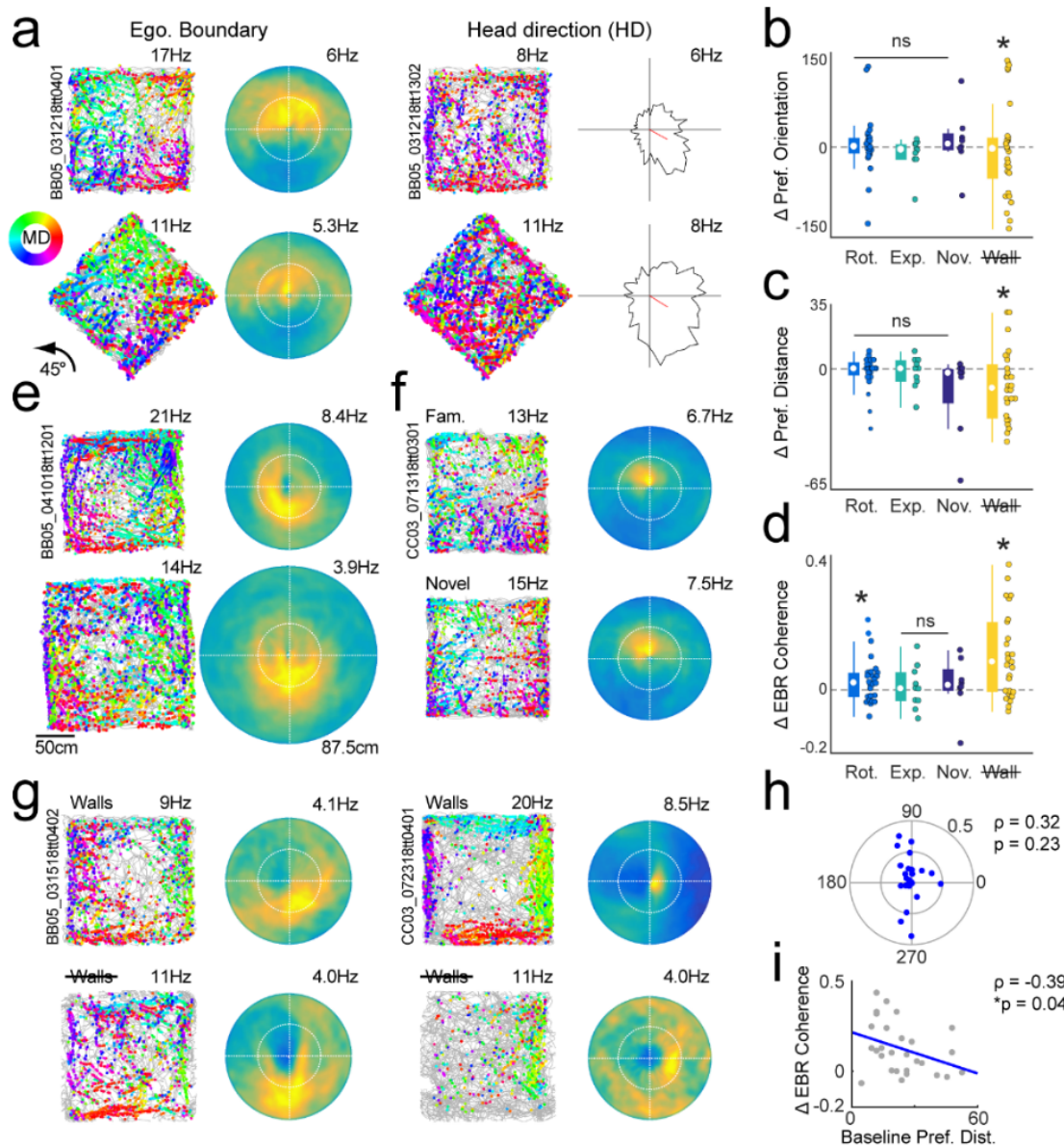
Figure 4. EBCs are anchored to local boundaries, respond in novel environments, and lose sensitivity in arenas without explicit borders. a. Left, trajectory plot and egocentric boundary ratemap (EBR) for an example EBC with similar egocentric boundary vector tuning in baseline experimental session (top) and a second session in an environment rotated 45° (bottom). Right, example head direction neuron sustains directional tuning across both conditions. **b.** Preferred orientation of EBC receptive fields in all arena manipulation sessions subtracted from preferred orientation in baseline sessions. **c.** Preferred distance of EBC receptive fields in all arena manipulation sessions subtracted from preferred distance in baseline sessions. **d.** EBC receptive field coherence in all arena manipulation sessions subtracted from receptive field coherence in baseline sessions. **e.** Trajectory plot and EBR for an example EBC with similar egocentric boundary vector tuning in baseline experimental session (top) and a second session in an expanded arena (bottom). **f.** Trajectory plot and EBR for an example EBC with similar egocentric boundary vector tuning in baseline experimental

1198   session (top) and a second session in a novel arena (bottom). **g.** Trajectory plot and EBR for
1199   two example EBCs between baseline session (top) and session with walls removed (bottom).
1200   Left EBC has a more distal receptive field and exhibits similar egocentric boundary vector
1201   tuning. Right EBC has a more proximal receptive field and has disrupted tuning in arena with no
1202   walls. **h.** For EBCs recorded in arenas without walls, the preferred orientation at baseline plotted
1203   against the change in EBC receptive field coherence between the two sessions. **i.** Same as **h,**
1204   but for change in coherence as a function of baseline preferred distance.
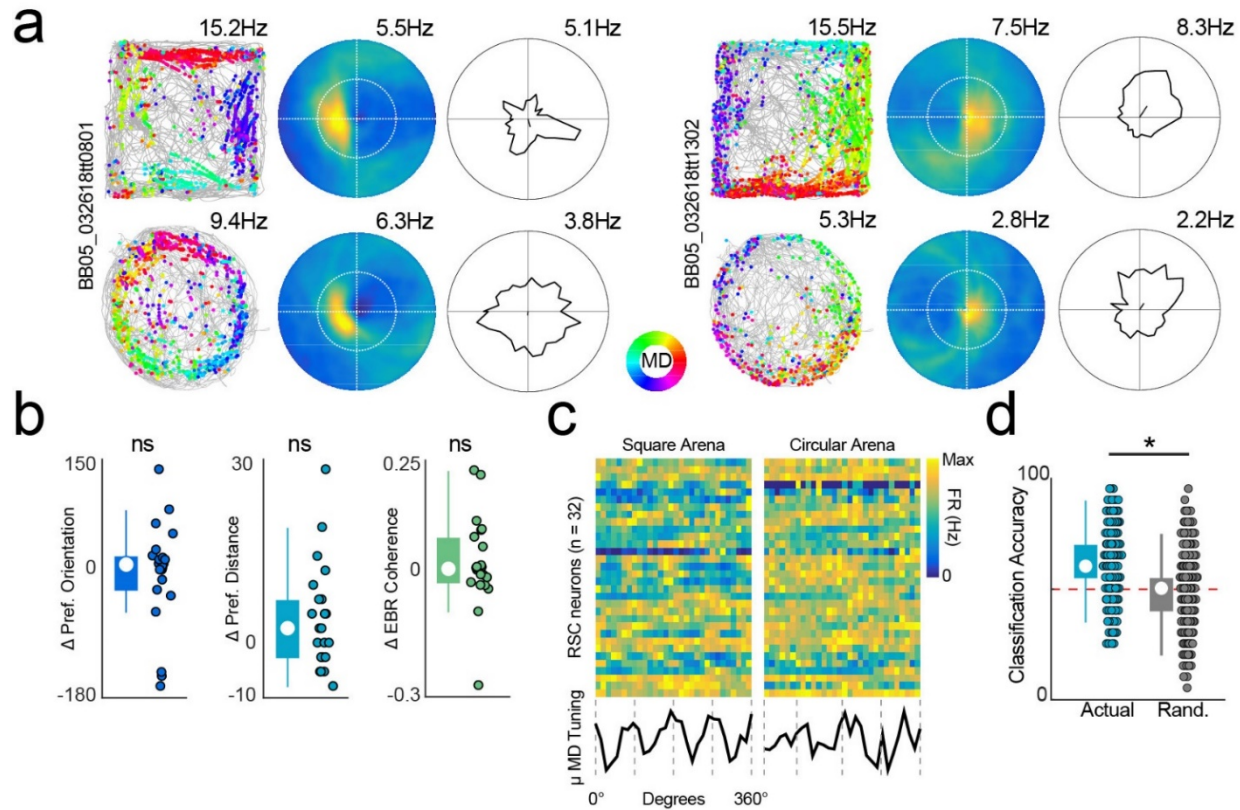
1205

1206

1207

1208

1209

1210

1211

1212

1213

1214

Figure 5. RSC EBCs are insensitive to environmental geometry which generates a directional representation of environment shape. a. Trajectory plots, egocentric boundary ratemaps (EBR), and movement direction tuning plots for two example RSC EBCs for experimental sessions in a square (top) and circular environment (bottom). **b.** Preferred orientation, preferred distance, and EBC receptive field coherence from recording sessions in the circular arena subtracted from the corresponding metrics in baseline sessions. **c.** Movement direction tuning plots for all RSC neurons in the square arena (left) and circular arena (right). Color depicts intensity of activation (blue is zero firing rate, yellow is maximum firing rate). Bottom in black, the average movement direction tuning across the full population of RSC neurons for the square and circular environments. Gray dashed lines depict 90° axes. **d.** Arena classification accuracy for linear discriminant analysis on movement direction tuning from **c**. In teal, actual classification. In gray, classification after randomizing arena identity. Red dashed line is statistical chance.

1233

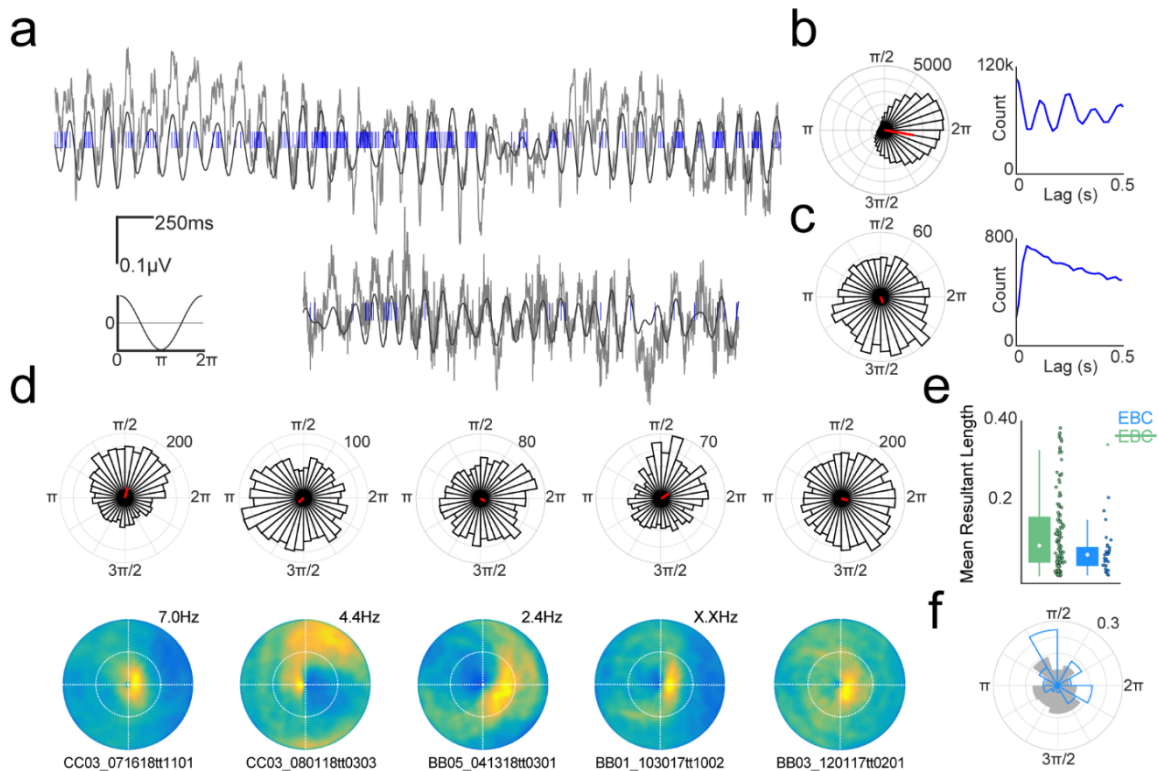**Figure 6. A subset of RSC EBCs are theta modulated. a.** Two examples of RSC theta oscillation (gray) and spike train of simultaneously recorded neurons (blue). Bottom left, scale bar and schematic depicting correspondence between oscillation and theta phase. **b.** Left, circular histogram depicting spike counts as a function of theta phase for the neuron in the top row of **a**. Density of spikes near 2π indicates that the neuron is locked to the peak of the theta phase. Right, spike train autocorrelogram for the same neuron shows theta rhythmic spiking. **c.** Same as in **b,** but for the neuron depicted in the bottom row of **a**. This neuron is significantly theta phase modulated but does not exhibit theta rhythmic spiking. **d**. Example theta phase modulated EBCs. Top row, circular histogram of spike counts versus theta phase. Bottom row, corresponding egocentric boundary ratemaps. **e.** Strength of theta phase modulation as measured by the mean resultant length for non-EBCs (green) and EBCs (blue). EBCs have significantly weaker theta modulation than non-EBCs with significant phase relationships. **f.** Preferred theta phase for all EBCs (blue) and non-EBCs (gray). EBCs tended to prefer the falling phase of the theta oscillation while non-EBCs preferred the rising phase but this difference was not significant.

1249 **Supplemental Figures**

1250
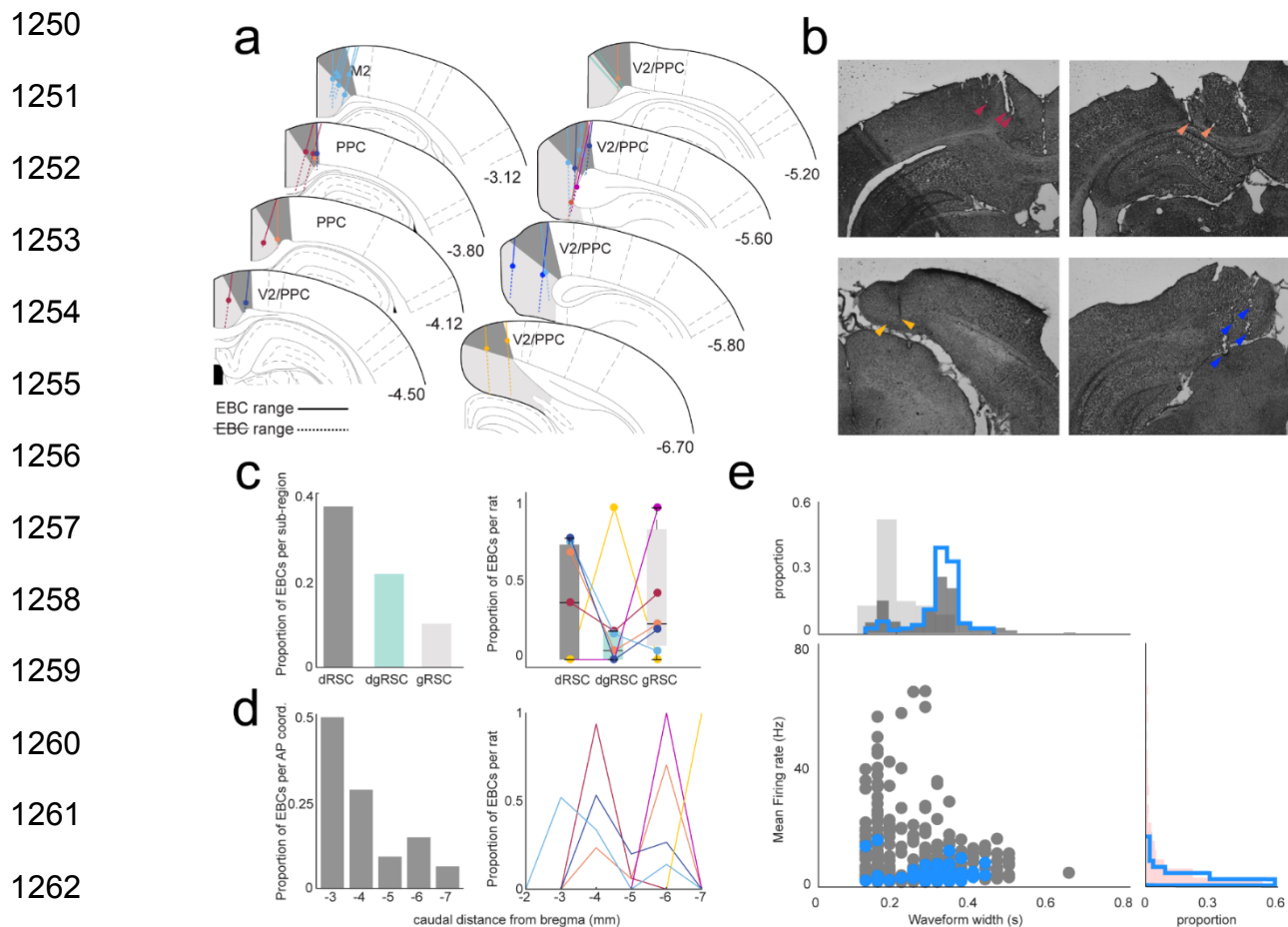
Supplemental Figure 1. Locations of RSC egocentric boundary cells and identification as putative principal cells. a. Schematic depicting location of tetrodes where EBCs were recorded. Each color corresponds to a different animal. Dark gray indicates dRSC and light gray indicates gRSC. Circles indicate the approximate dorsal-ventral (D/V) position of the wire for the last recording with EBCs on each tetrode. The dashed line indicates span of recordings in D/V axis that did not yield EBCs. Solid line indicates span of recordings in D/V axis that did yield EBCs. EBCs were also observed in secondary motor cortex (M2) or parietal cortex (V2/PPC) and these regions are noted. **b.** Example histology showing tetrodes in RSC. Tetrode locations are indicated with colored triangles which correspond to individual animals in **a**. **c.** Left, proportion (out of 1.0) of EBCs relative to all RSC neurons recorded in each RSC sub-region. Right, proportion of EBCs relative to all RSC neurons recorded in each sub-region for each animal (colored dots and lines). **d.** Same as for **c**, but for approximate anterior-posterior location of EBC. **e.** Bottom left, scatterplot depicting mean firing rate versus width of spike waveform for all RSC neurons in gray and EBCs in blue. Top, histogram of waveform width clustered into fast (light gray) and slow waveforms (dark gray). Blue histogram corresponds to distribution of waveform width for all EBCs which have wider waveform widths. Right, histogram of mean firing rate (light pink). Blue histogram corresponds to distribution of mean firing rate of all EBCs demonstrating overall low mean firing rate.
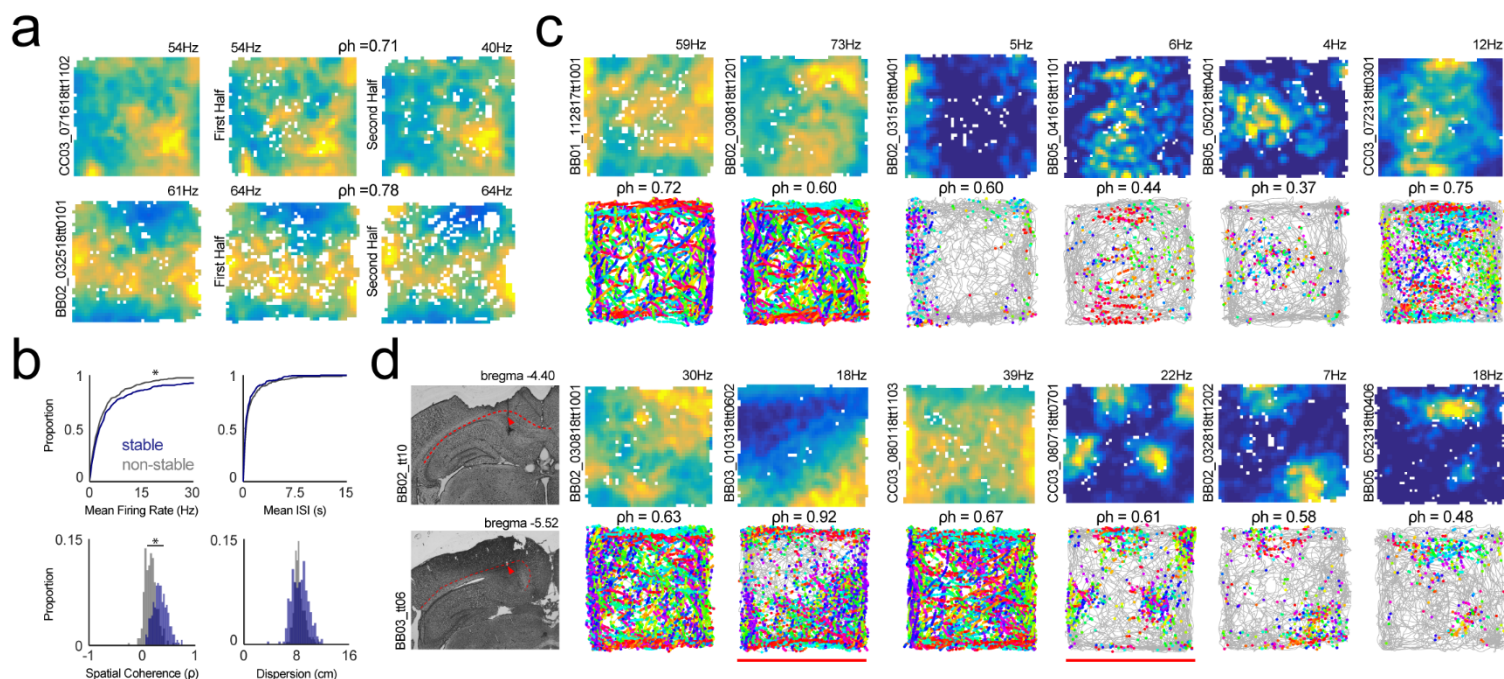
1281

Supplemental Figure 2. RSC spatial stability during free foraging. a. Two-dimensional (2D) firing ratemaps for two neurons (rows) showing process for determining spatial stability. Left column, 2D ratemap for full session. Middle and right columns, 2D ratemaps for the first and second halves of each session. Above ratemaps, corresponding spatial correlations between the two halves of the session. **b.** Properties of spatially stable (blue) versus non-stable (gray) RSC neurons. Top left, spatially stable cells had slightly lower mean firing rates than those that did not have spatial reliability (**sFigure2b;** stable = 3.02, IQR = 1.23 - 7.25Hz; not-stable = 4.93, IQR =0.95 - 5.56Hz; Wilcoxon rank sum, z= -1.06, p = 0.04). Top right, mean inter spike intervals were not different between stable and non-stable neurons (stable = 0.36, interquartile range (IQR) = 0.15 - 0.99; non-stable = 0.41, IQR = 0.19 - 1.15; Wilcoxon rank sum, z = 1.89, p = 0.06). Bottom left, RSC neurons with spatially reliable activity had significantly greater spatial coherence than non-stable cells (stable Spearman's ρ = 0.33, IQR = 0.25 - 0.43; not-stable Spearman's ρ = 0.16, IQR =0.08 - 0.23; Wilcoxon rank sum, z= -14.448, p = 2.6x10^{-47}). Bottom right, spatial dispersion of the top 90% of firing rate bins in centimeters for stable and non-stable neurons (stable = 21.3cm, interquartile range (IQR) = 18.8 - 23.3cm; non-stable = 20.6cm, IQR = 19.7 - 22.2cm; Wilcoxon rank sum, z = 1.89, p = 0.06). **c.** 2D ratemaps and trajectory plots for example RSC neurons with significant spatial stability. **d.** Example 2D firing rate maps and trajectory plots for neurons recorded at or near the cingulum bundle. Left column shows two such recording locations with neurons recorded at each site demarcated with a horizontal red line. In some cases, recordings from the cingulum bundle resembled grid cells.
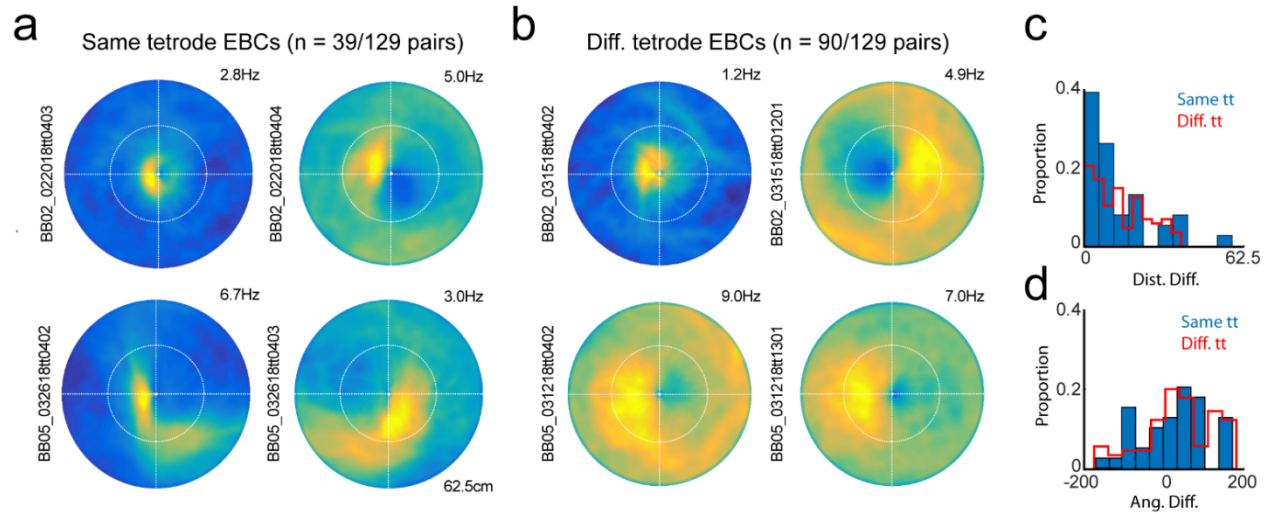
1302

1303

1304

1305

1306

Supplemental Figure 3. Simultaneously recorded egocentric boundary cells. a. Each row depicts egocentric boundary ratemaps for a pair of simultaneously recorded egocentric boundary cells that were observed on the same recording tetrode. Top pair have similar EBC receptive field locations while bottom pair have receptive fields on different sides of the animal. **b.** Same as in **a**, but for simultaneously recorded neurons on different tetrodes. Top pair have different receptive field locations while bottom pair have similar receptive fields. **c.** Histogram of absolute difference in preferred distance for pairs of simultaneously recorded EBCs on the same tetrode (in blue) and on different tetrodes (in red). **d.** Histogram of difference in preferred orientation for pairs of simultaneously recorded EBCs on the same tetrode (in blue) and on different tetrodes (in red).

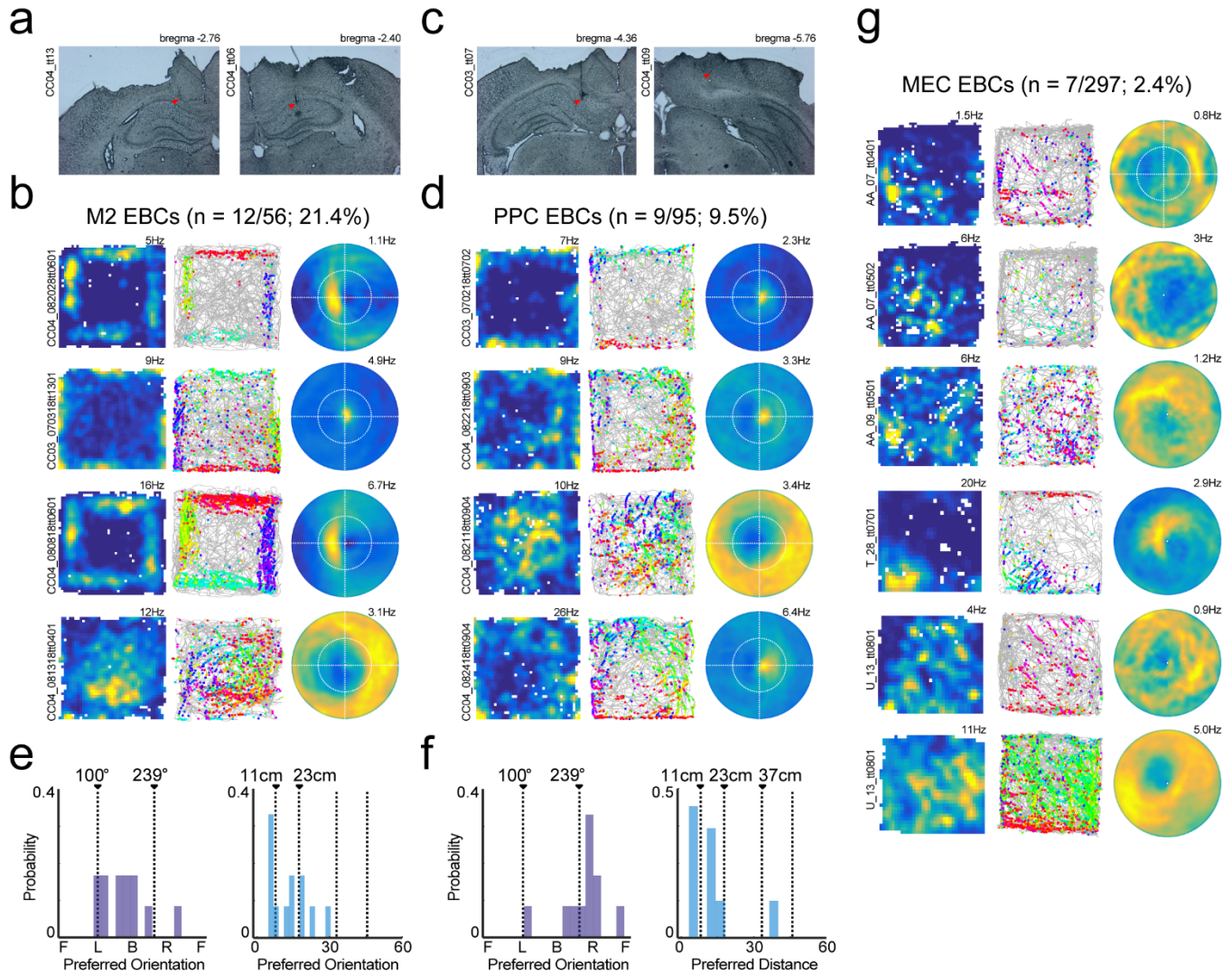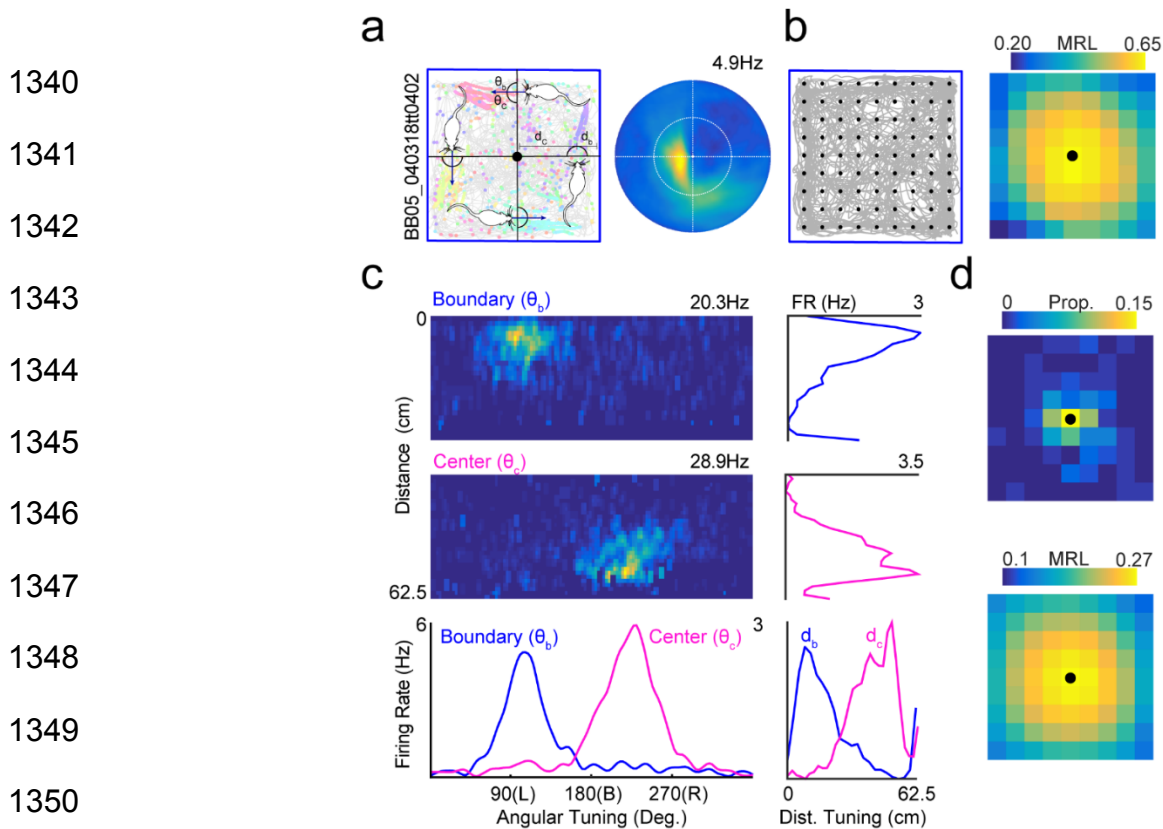**Supplemental Figure 4. Egocentric boundary cells in secondary motor cortex and posterior parietal cortex but not medial entorhinal cortex. a.** Example histology showing placement of recording tetrodes in secondary motor cortex (M2). **b.** 2D ratemaps, trajectory plots and egocentric boundary ratemaps (EBR) for 4 example M2 neurons with EBC sensitivity. **c.** Example histology showing placement of recording tetrodes in parietal cortex (V2/PPC). **d.** 2D ratemaps, trajectory plots and egocentric boundary ratemaps (EBR) for 4 example V2/PPC neurons with EBC sensitivity. **e.** Preferred orientation and distance for M2 neurons identified as EBCs. **f.** Preferred orientation and distance for V2/PPC neurons identified as EBCs. **g.** All detected medial entorhinal cortex EBCs.

Supplemental Figure 5. Egocentric vector tuning to center of arena for generalized linear models. a. Left, schematic depiction of the angular and distance relationships between the animal, the boundary, and the arena center when the animal is running parallel to arena walls. Right, egocentric boundary ratemap for an EBC with trajectory plot on left plot. **b.** To analyze whether the egocentric bearing and distance to the arena center could function as a predictor in generalized linear modelling we analyzed strength of egocentric bearing and distance tuning to a 9x9 grid of locations that spanned the entirety of the environment (see Wang, Chen, et al., 2018). Right plot depicts the strength (as measured by mean resultant length, MRL) of egocentric vector tuning to all 9x9 grid locations for the neuron depicted in **a.** The heatmap corresponds to magnitude of the MRL, and the black dot depicts the grid location with the strongest egocentric tuning which, in this case, corresponds to the center of the arena. **c.** For the same neuron we calculated egocentric bearing and distance tuning to the nearest point on the boundary (top left EBC heatmap) and the grid location with maximum tuning (center of arena, bottom left EBC heatmap), and compared their vector components by averaging across angular and distance dimensions of each matrices. Plots to the right of each EBC heatmap show average distance tuning to the nearest boundary (blue) and center (pink) with each overlaid on the bottom right plot. Below the EBC heatmaps are overlaid averages of preferred angular tuning for nearest boundary (blue) and arena center (pink). The tuning plots at the bottom for both reference points show a clear relationship and so we utilized the egocentric boundary and distance to the central location for GLM analyses. **d.** Top, 2D histogram showing the proportion of RSC EBCs with maximum MRLs at each grid location. Greatest proportion is at or near the center of the arena in baseline sessions when boundaries are excluded. Bottom, mean MRL tuning for all grid locations across all RSC EBCs shows maximum egocentric vector tuning to the arena center in baseline sessions when boundaries are excluded.
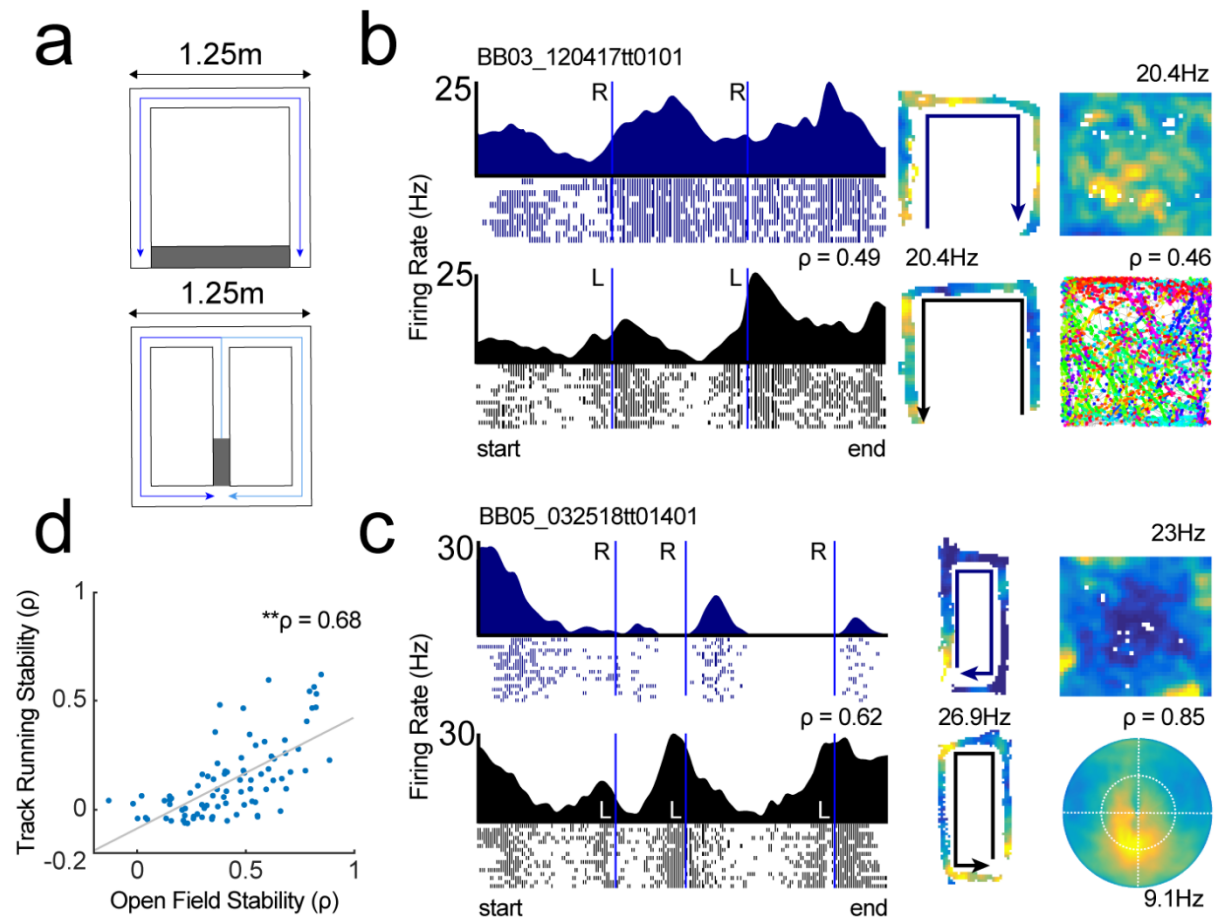
Supplemental Figure 6. Comparison between RSC neurons recorded in free foraging and during track running. a. Schematic of two different tracks animals ran along. Gray zone indicates reward location. **b**. Linearized firing rate vectors split into left-turning and right-turning routes with corresponding 2D ratemaps for two RSC neurons. Left column in blue, mean firing rate for route with right turns and trial spike trains. Left column in black, mean firing rate for route with left turns and trial spike trains. 2D ratemaps for track running depicted in middle column. Right column, 2D ratemap and trajectory plot. **c.** Same as **b**, but right column depicts 2D ratemap and corresponding egocentric boundary ratemap. This neuron shows spatial selectivity on track near turns and is an egocentric boundary neuron in the open field. Critically, the EBC receptive field does not explain apparent counterclockwise (left) turning preference on the track. **d.** Scatterplot depicting Spearman's ρ for open field stability versus track running stability for all RSC neurons recorded in both conditions. Significant positive correlation indicates that neurons that were stable in one condition were more likely to be stable in the other.

1393 **Methods**

1394 **Subjects.** Male Long-Evans rats (n = 7; Charles River Labs, Wilmington, MA) were housed

1395 individually in plexiglass cages and kept on a 12-h light/dark cycle. Rats had continuous access

1396 to food during a habituation period lasting approximately 1 week. After this period, animals were

1397 food restricted until they reached 85-95% of their weight during free feeding. Water was

1398 available continuously. All procedures were approved by the Institutional Animal Care and Use

1399 Committee at Boston University.

1400 **Shaping/behavior.** Animals were acclimated to the primary testing room for approximately one

1401 week. During acclimation, rats were handled by multiple researchers and trained to consume

1402 both Froot Loops (General Mills, Battle Creek, MI) and 45mg chocolate pellets (Bio-Serv,

1403 Flemington, NJ). After animals readily ate both food items they were exposed to one of two

1404 familiar open fields used for baseline sessions for 20 to 45 minutes per day. The first open field

1405 was $1.25m^2$ with four black walls 30 cm in height. The second arena was $1.25m^2$ with three black

1406 walls and one white wall 30 cm in height. Both arenas were placed on a dark gray textured

1407 rubber floor that was cleaned between sessions. Two animals (BB01 and BB03) performed a

1408 goal directed navigation task in a different arena and testing room prior to being utilized for the

1409 current study.

1410 **Surgical procedures.** Rats were surgically implanted with custom-fabricated hyperdrives in

1411 aseptic conditions. Each hyperdrive was composed of 12 to 16 nickel chromium tetrodes (12μm,

1412 Kanthal-Sandvik, Hallstahammar, Sweden) that could be independently moved in as small as

1413 35μm increments. Guide cannulae for each tetrode were collectively configured in one of three

1414 arrays: 1) filling a single hypodermic tube approximately $2mm^2$ in diameter, 2) across two

1415 conjoined hypodermic tubes that were $\sim1.5mm^2$ in diameter spanning a total of ~3mm or, 3)

1416 across four conjoined hypodermic tubes that were $\sim1.25mm^2$ in diameter and spanned a total of

1417 ~5mm. For the second and third configurations, the long axis of the electrode array was

1418 positioned to target an extended region of the anterior-posterior axis of retrosplenial cortex.

1419 Animals were anesthetized using a combination of inhaled isoflurane (0.5% initial concentration)

1420 and ketamine/xylazine administered via intraperitoneal injection (Ketamine: 12.92 mg/kg,

1421 Acepromazine: 0.1mg/kg, Xylazine: 1.31 mg/kg). After the animal was determined to be under

1422 anesthesia (as assessed via loss of the toe pinch reflex), the animal was positioned in a

1423 stereotaxic apparatus, a 0.1mg/kg dose of atropine was administered subcutaneously, and the

1424 head was shaved. Excess hair was removed via application of Nair (Church & Dwight Co.,

1425 Ewing, NJ) and the scalp was cleaned with 70% ethanol and Betadine (Avrio Health L.P.,

1426   Stamford, CT). 0.9% sodium chloride was administered subcutaneously hourly throughout the

1427   surgical procedure.

1428   Following a midline incision and subsequent clearing of connective tissue, a ground screw was

1429   positioned above the cerebellum and 5-8 anchor screws were affixed in an array around the

1430   perimeter of the exposed skull. A large craniotomy was centered above retrosplenial cortex

1431   (relative to bregma: A/P: -2mm to –7mm; M/L ±0mm-1.75mm). The exact size and position of

1432   the craniotomy was dependent upon the aforementioned configuration of the hyperdrive array.

1433   Next, dura was resected and the hyperdrive was positioned such that guide cannula rested

1434   gently against the dorsal surface of the brain. Excess exposed tissue within the craniotomy was

1435   protected with Kwik-Sil (World Precision Instruments, Sarasota, Fl), and the implant was

1436   secured to anchor screws with dental cement. Tissue around the implant was cleaned with

1437   saline, 70% ethanol, and hydrogen peroxide. Antibiotic ointment was applied into the wound,

1438   sutured if necessary, and Neosporin was applied around the site. Prior to removal from

1439   anesthesia tetrodes were lowered approximately 0.25mm D/V. Animals received post-operative

1440   antibiotics (Baytril: 10mg/kg) and analgesics (Ketofen: 5.0mg/kg) for five days after surgery and

1441   were freely fed. After one-week post-operation animals were handled and reacclimated to the

1442   testing room and free foraging environments prior to the initiation of experiments.

1443   **Electrophysiological recordings.** Neural signals were amplified at two headstages attached to

1444   a 64 channel electrical interface board and acquired by a 64 channel Digital Lynx acquisition

1445   system (Neuralynx, Bozeman, MT) Signals were digitized, filtered (0.3-6.0kHz), and amplified

1446   (5,000-20,000X). Timestamps of individual action potentials were detected online when the

1447   signal crossed an acquisition threshold on any individual electrode composing a tetrode. At the

1448   conclusion of each experiment, spikes were manually sorted to individual single units using

1449   Offline Sorter (Plexon Inc., Dallas, TX) and the following features: peak-valley, peak, and

1450   principal components 1-3. Two diodes attached to the electrode implant delineated the location

1451   of the animal which was tracked at 30Hz via a camera positioned above the recording arena.

1452   An experimental session began with an initial 15-30 minute recording while the animal free

1453   explored and consumed either Froot Loops scattered by an experimenter, chocolate pellets

1454   released at random intervals from a dispenser positioned above the arena, or both (Open Ephys

1455   Pellet Dispenser designed by Maurer Lab, https://github.com/jackpkenn/PelletDispenser). After

1456   adequate spatial coverage was achieved the animal was removed from the arena and placed

1457   back in its home cage for a period of 1 hour minimally. During this period, the experimenter

1458   completed clustering of action potentials into single neurons and examined two-dimensional

1459   spatial ratemaps (described below) to assess whether any of the cells from the baseline session

1460   exhibited egocentric boundary vector sensitivity. If no EBCs were present, tetrodes were

1461   typically lowered between 35 and 70µm. If EBCs were present, a second experimental session

1462   was conducted in which the animal explored an open field in one or more of the following

1463   configurations:

1464   1) Open field session: The same arena from the baseline session to assess the stability of

1465   EBCs in familiar environments.

1466   2) Open field rotation: The same arena from the baseline session rotated 45° relative to the

1467   testing room and all visible distal cues present therein.

1468   3) Circular open field: A familiar circular arena of 1.1m diameter.

1469   4) Open field expansion or contraction: If an expansion experiment was planned the initial

1470   baseline session was conducted in a familiar 1.25m^2 arena that enabled reconfiguration

1471   of walls. Following the baseline session, walls were uniformly moved outwards relative to

1472   the center point of the baseline configuration to a size of 1.5m^2 or larger. In a small

1473   number of recordings, walls were either: moved non-uniformly to increase the length of

1474   the arena along a single axis of the environment or, contracted to decrease the size of

1475   the environment. Across all possible wall movements, the arena was altered in size by

1476   approximately 20% along each dimension.

1477   5) No wall open field: If a no wall arena experiment was planned the initial baseline session

1478   was conducted in a familiar 1.25m^2 environment that was placed approximately 20cm

1479   above the floor. Following this session, the walls were removed from this arena creating

1480   a platform with no walls that the rat explored for a second time. In a small number of

1481   sessions, the animal explored the familiar 1.25m^2 that was situated on the testing room

1482   floor, then in a second session, explored a different familiar arena lacking walls placed

1483   approximately 8" above the floor.

1484   All arenas were positioned such that the animal could easily see the broader recording room

1485   and an array of stable distal cues. In some cases, the manipulation session was followed by a

1486   return session to the familiar baseline arena.

1487   **Histology.** Animals were anesthetized with 0.5% isoflurane and small electrical lesions were

1488   made at the end of tetrodes that had preliminarily been identified as having EBCs. After one

1489   week, animals were deeply anesthetized with isoflurane, injected with sodium pentobarbital, and

1490   transcardially-perfused with 0.9% saline followed by 10% formalin. The brain was extracted from

1491   the skull and post-fixed overnight with 10% formalin, then stored in 0.1M phosphate buffer until

1492   two days before slicing when it was transferred to a 0.1M phosphate buffer/30% sucrose

1493   solution. The brain was snap frozen using 2-methylbutane and sliced into 40-50um coronal

1494   sections using a cryostat (Leica CM3050S, Leica Biosystems, Buffalo Grove, IL). Slices were

1495   mounted on gelatin covered microscope slides and allowed to dry, then photographed (Nikon

1496   DXM1200 camera mounted on Olympus BX51 light microscope). Tetrode lesions and tracts

1497   were clearly visible in all animals. Coordinates of tetrode locations and final tetrode depths were

1498   registered with respect to pre-implant photographs of guide cannulae array configurations and

1499   tetrode turning logs, respectively.

1500   **Data Analysis**

1501   *Two-dimensional (2D) spatial ratemaps and spatial stability.* Animal positional occupancy within

1502   an open field was discretized into 3x3cm spatial bins. For each neuron, the raw firing rate for

1503   each spatial bin was calculated by dividing the number of spikes that occurred in a given bin by

1504   the amount of time the animal occupied that bin. Raw firing rate maps were smoothed with a 2D

1505   Gaussian kernel spanning 3cm to generate final rate maps for visualization. Individual raw firing

1506   rate maps were also computed after dividing the session into halves. To assess spatial stability

1507   of an individual RSC neuron, the similarity of the two raw firing rate maps from non-overlapping

1508   halves of the recording session was calculated using the non-parametric Spearman's rank

1509   correlation coefficient. To determine whether a given spatial stability value was greater than

1510   expected by chance we next conducted randomization tests wherein the spike train for each

1511   RSC neuron was circularly shifted relative to spatial position 100 times, and individual firing rate

1512   maps were constructed for non-overlapping halves that were then correlated. The spatial

1513   stability correlation values following randomizations were collapsed into a single distribution for

1514   all neurons and randomizations and the 99th percentile of all values was calculated. RSC

1515   neurons with real spatial stability correlations greater than this threshold were determined to

1516   have robust two-dimensional spatial stability.

1517   *Construction of egocentric boundary ratemaps.* Egocentric boundary ratemaps (EBR) were

1518   computed in a similar manner as 2D spatial ratemaps but referenced relative to the animal

1519   rather than the spatial environment. The position of the boundaries relative to the animal was

1520   calculated for each position sample (i.e. frame). For each frame, we found the distance, in

1521   2.5cm bins, between arena boundaries and angles radiating from 0° to 360° in 3° bins relative to

1522   the rat's position. Critically, angular bins were referenced to the current movement direction of

1523   the animal such that 0°/360° was always directly in front of the animal, 90° to its left, 180°

1524   directly behind it, and 270° to its right. Intersections between each angle and environmental

1525   boundaries were only considered if the distance to intersection was less than or equal to ½ the

1526   length of the most distant possible boundary (in most cases this threshold was set at 62.5cm or

1527   half the width of the arena). In any frame the animal occupied a specific distance and angle

1528   relative to multiple locations along the arena boundaries, and accordingly, for each frame, the

1529   presence of multiple boundary locations were added to multiple 3° x 2.5cm bins in the

1530   egocentric boundary occupancy map. The same process was completed with the locations of

1531   individual spikes from each neuron, and an EBR was constructed by dividing the number of

1532   spikes in each 3° x 2.5cm bin by the amount of time that bin was occupied in seconds.

1533   Smoothed EBRs were calculated by convolving each raw EBR with a 2D Gaussian kernel (5 bin

1534   width, 5 bin standard deviation).

1535   For EBR construction and other analyses in the current work, movement direction was defined

1536   as the instantaneous derivative of the position signal whereas head direction was the

1537   instantaneous angle calculated from the location of two position tracking diodes. Movement

1538   direction was utilized as the primary directional variable in EBR construction but a comparison

1539   to head direction determined the latter to be a less robust signal for egocentric boundary vector

1540   tuning.

1541   *Head direction cell identification.* For each neuron, the mean resultant length of the firing rate as

1542   a function of head direction was calculated as

1543
$$R_m = \frac{\cos(\bar{\theta}) \sum_{i=1}^{n} F_i \cos(\theta_i) + \sin(\bar{\theta}) \sum_{i=1}^{n} F_i \sin(\theta_i)}{\sum_{i=1}^{n} F_i}$$

1544   where $\bar{\theta}$ was the head direction of firing and F_i and θ_i were the firing rate and head direction for

1545   bin i. Head direction cells (HD) were identified as those cells with R_m greater than 0.20. HD cells

1546   (n = 27/555; 4.9% of all RSC neurons) were removed from the possible pool of RSC EBCs.

1547   *Identification of neurons with egocentric boundary vector tuning.* To identify neurons with

1548   significant egocentric boundary vector sensitivity we began by calculating the mean resultant

1549   (MR) of the cell's egocentric boundary directional firing collapsed across distance to the

1550   boundary. The mean resultant was calculated as

1551
$$MR = \left(\sum_{\theta=1}^{n} \sum_{D=1}^{m} F_{\theta,D} * e^{i*\theta} \right) / (n * m)$$

1552   where θ is the orientation relative to the rat, D is the distance from the rat, $F_{\theta,D}$ is the firing rate in

1553   a given orientation-by-distance bin, n is the number of orientation bins, m is the number of

1554   distance bins, e is the Euler constant and i is the imaginary constant. The MRL is defined as the

1555   absolute value of the mean resultant and characterized the strength of egocentric bearing tuning

1556   to environment boundaries. We next computed the preferred orientation of the egocentric

1557   boundary ratemap as the mean resultant angle (MRA)

1558
$$MRA = arctan2\left(\frac{imag(MR)}{real(MR)}\right)$$

1559   We estimated the preferred distance by fitting a Weibull distribution to the firing rate vector

1560   corresponding to the MRA and finding the distance bin with the maximum firing rate. The MRL,

1561   MRA, and preferred distance were calculated for each neuron for the two halves of the

1562   experimental session independently. Next, the MRL was computed for each neuron following 100

1563   random, unrestricted, circular shifts of the spike train relative to position. The 99th percentile of the

1564   MRL distribution across all neurons was determined.

1565   A neuron was characterized as having egocentric boundary vector tuning (i.e. an EBC) if it

1566   reached the following criteria: 1) the MRL for both halves of the baseline session were greater

1567   than the 99th percentile of the randomized distribution, 2) the absolute circular distance in

1568   preferred angle between the 1st and 2nd halves of the baseline session was less than 45°, and 3)

1569   the absolute difference in preferred distance between the 1st and 2nd halves of the baseline

1570   session was less than 75% of the preferred distance for the entire session.

1571   To refine our estimate of the preferred orientation and preferred distance of each neuron we

1572   calculated the center of mass (COM) of the receptive field defined after thresholding the entire

1573   EBR at 75% of the peak firing and finding the largest continuous contour ('contour' in Matlab).

1574   We repeated the same process for the inverse EBR for all cells to identify both an excitatory and

1575   inhibitory receptive field and corresponding preferred orientation and distance for each neuron.

1576   *Clustering of EBC receptive field sub-types.* In an effort to identify trends in receptive field sub-

1577   types including those exhibiting inverse receptive fields, we next clustered the EBC sub-

1578   population using k-means ('kmeans' in MATLAB) and the following feature space: distance from

1579   the origin to the global minimum of the EBR, distance from the origin to the global maximum of

1580   the EBR, the stepwise percentage of the EBR that was greater than 20% to 90% of the

1581   maximum firing rate in 10% bounds, and the dispersion of the EBR and inverse EBR. All

1582   features were z-score normalized across the population of EBCs prior to clustering. K-means

1583   was run on these features for up to 10 clusters and the total within-cluster sums of point-to-

1584   centroid distances (SUMD) were examined to assess which K was appropriate for the current

1585   data. Repeated iterations of k-means clustering and qualitative inspection of the K vs SUMD

1586   plot revealed a consistent elbow at K = 4 clusters. Principal components analysis ('pca', in

1587   MATLAB) was run on the same features to visualize whether k-means was partitioning distinct

1588   clusters or a continuum.

1589   *Ratemap coherence, dispersion, and receptive field size.* For either egocentric boundary

1590   ratemaps or 2D spatial ratemaps, coherence was defined as the Spearman's correlation

1591   between each spatial bin and the mean firing rate of all adjacent bins. Dispersion was calculated

1592   as the mean within rate map distance of the top 10% of firing rate bins. Receptive field size was

1593   only calculated for egocentric boundary ratemaps (described below), and was defined by the

1594   area (percentage of all egocentric boundary ratemap degree x cm bins) of the largest single

1595   contour detected after selecting for bins with firing rates greater than 75% of the maximum firing

1596   rate.

1597   *Self-motion rate maps and assessment of self-motion sensitivity.* Angular displacement (θ) was

1598   calculated by determining the circular difference in movement direction between two position

1599   samples (frames) separated by a 100ms temporal window. The total distance (d) traveled

1600   between these two frames was also calculated. The process was repeated for the full recording

1601   by sliding a 100ms temporal window across all position frames and calculating these values.

1602   Angular displacement and distance traveled were converted to Cartesian coordinates to

1603   generate x- and y-displacement values in centimeters, which corresponded to lateral and

1604   longitudinal displacements for each frame across the full recording.

1605   Two-dimensional displacements were binned (1cm) and convolved with a two-dimensional

1606   Gaussian spanning 3cm. For each neuron, the same process was repeated for displacement

1607   values that co-occurred with spike times to generate a spike occupancy map as a function of

1608   displacement. Self-motion rate maps were constructed by dividing the spike occupancy map for

1609   each neuron by the total time in each displacement bin. Bins occupied for less than 267ms were

1610   removed from analyses as they typically were observed at extreme displacement values. Self-

1611   motion ratemaps for each neuron were additionally constructed independently from interleaved,

1612   non-overlapping, 1 second periods throughout the entire session to assess stability of self-

1613   motion tuning. For quantification of self-motion tuning relative to a randomized distribution, all

1614   aforementioned ratemaps were generated for each neuron 100 times after randomly shifting the

1615   spike train relative to position.

1616 Self-motion ratemaps were quantified for their stability, left- versus right-turning preference, and
1617 speed modulation. First, stability of self-motion tuning was quantified by correlating self-motion
1618 ratemaps generated from non-overlapping periods for each neuron (**Figure 2c**). Next, turning
1619 biases for clockwise versus counterclockwise movements (LvR FR ratio, **Figure 2d**) were
1620 quantified by computing the ratio of summated firing for all displacement bins on the right side
1621 and left side of the zero vertical line, respectively. Finally, speed modulation was assessed by
1622 finding the mean firing rate as a function of longitudinal displacement (i.e. averaging over
1623 columns of self-motion ratemaps) and correlating with the y-displacement value (**Figure 2e**). All
1624 self-motion ratemap quantification was repeated for all randomized self-motion ratemaps as
1625 mentioned above. Stability and turn-bias quantification were computed from displacement bins
1626 that were occupied in both self-motion ratemaps or both halves of an individual self-motion
1627 ratemap. All quantification was completed on non-smoothed self-motion ratemaps.

1628 *Generalized linear models.* In order to more directly test to what degree these neurons
1629 represented egocentric compared to allocentric variables, we adopted a generalized linear
1630 model framework. The probability of spiking in a given behavioral frame (33Hz) is described by
1631 an inhomogeneous Poisson process, where the probability of spiking in a given frame is
1632 described by the time varying variable λ:

1633
$$P(Spike \mid t) = e^{-\lambda(t)}$$

1634
$$\lambda(t) = \lambda_{FR} * \lambda(t)_{SelfMovement} * \lambda(t)_{Egocentric}$$

1635 Where:

1636
$$\lambda_{FR} = \beta_0$$

1637
$$\lambda_{SelfMovement}(t) = v_1 S + v_2 A$$

1638
$$\lambda_{Allocentric}(t) = \rho_1 x + \rho_2 y + \rho_3 x^2 + \rho_4 y^2 + \rho_3 xy + \rho_6 \cos(\varphi) + \rho_7 \sin(\varphi)$$

1639
$$\lambda_{Egocentric}(t) = \varepsilon_1 d + \varepsilon_2 d^2 + \varepsilon_3 \sin(\theta) + \varepsilon_4 \cos(\theta) + \varepsilon_5 d * \sin(\theta) + \varepsilon_6 d * \cos(\theta)$$

1640 Where β_0 defines the baseline firing rate of the neuron. All subscripted variables are fit
1641 coefficients weighting the other (time-varying) variables. S is the running speed of the animal
1642 and A is the angular displacement of the animal, as described above. X and y are
1643 measurements of the animal's position in the environment in pixels, and φ is the movement
1644 direction. Finally, d is the animal's distance from the center of the environment, and θ is the
1645 egocentric angle to the center of the environment.

1646   Coefficients were determined by fitting to maximize log-likelihood (MATLAB function `glmfit`) of

1647   the experimental spike train given the behavioral variables. For statistical tests, some number of

1648   the coefficients were set to zero, giving a log-likelihood for the reduced model. The difference in

1649   likelihood for the full versus reduced model was compared to a Chi-Square distribution (degrees

1650   of freedom equal to the number of coefficients set to zero) to generate an analytic p-value.

1651   While theoretically the change in log-likelihood should follow a Chi-Square distribution, this is

1652   only the case when the spike train has been fit very well (eg: including all neuron-neuron

1653   coupling terms). In line with previous approaches, we therefore also compared the change in

1654   log-likelihood in two additional manners. First, we compared the change in log-likelihood to that

1655   from 1000 randomly shuffled spike train, giving an empirical null-distribution. Secondly, when

1656   comparing the relative effects of two variables (that is, comparing two reduced models to each

1657   other), we can derive the difference in Akaike Information Criteria (dAIC) for each of the reduced

1658   models, and compare their magnitudes. Example spike trains for each model were generated by

1659   evaluating lambda for each behavioral time point ('glmeval') and using this as the input to a

1660   random Poisson Generator ('poissrnd').

1661   *Assessment of theta-phase modulation.* For each experimental session an LFP channel was

1662   identified that was qualitatively noise free. The LFP signal was filtered in the theta frequency

1663   range (6-10Hz) and the phase for each spike from each neuron was estimated as the

1664   instantaneous phase angle of the corresponding Hilbert transform ('hilbert' in Matlab). For each

1665   neuron, the MRL and MRA were calculated on the full spike phase distribution using the circular

1666   statistics toolbox (Berens et al., 2009; MRL, 'circ_r'; MRA, 'circ_mean'). We next randomly

1667   shifted the spike train relative to theta phase 100 times for each neuron to generate a null

1668   distribution of MRL values. RSC neurons with MRLs greater than the 95th percentile of the full

1669   distribution of randomized MRL values were determined to be theta-phase locked.

1670   *Assessment of theta rhythmic spiking.* Spike train autocorrelograms were estimated by

1671   generating a histogram of temporal lags between spikes in a 400ms temporal window

1672   discretized into 20ms bins. For each neuron, the power spectrum of the autocorrelogram was

1673   computed using the Fourier transform ('fft' in Matlab) and the peak in the theta frequency range

1674   was identified (if it existed). If the mean power within 1Hz of this theta peak was 50% greater

1675   than the mean power for the full power spectrum, the neuron was determined to exhibit intrinsic

1676   theta spiking.

1677   *Gaussian Mixture Models.* Preferred orientation and preferred distance estimates were modeled

1678   as mixtures of Gaussian distributions using orders from 1 to 10 ('fitgmist' in Matlab). Optimal

1679   models were identified as those that minimized the Akaike information criterion (AIC). The mean

1680   of each Gaussian component is reported and a probability distribution function of the optimal

1681   model was generated to visualize mixture model fit ('pdf' in Matlab).

1682   *Statistics.* Unless otherwise stated, non-parametric tests with a p-value threshold at 0.05 were

1683   utilized for all statistical comparisons. Median and interquartile range are provided for all

1684   distributions in which comparisons were made.

1685   *Data and code availability.* The toolbox used for alignment of behavioral and spike data, along

1686   with basic analysis is available at https://github.com/hasselmonians/CMBHOME. The toolbox

1687   used for egocentric boundary rate map generation and related analyses is available at

1688   https://github.com/hasselmonians/rscOpenFieldTuning (to be made public before journal

1689   acceptance). The toolbox used for GLM fits, evaluation, and spike-train generation is available

1690   at https://github.com/wchapman/pippin (to be made public before journal acceptance).